THE PENNSYLVANIA STATE UNIVERSITY
SCHREYER HONORS COLLEGE

DEPARTMENT OF ENGINEERING SCIENCE AND MECHANICS

SPIN AND ORBITAL ANGULAR MOMENTUMS OF MULTIPLE TRAINS OF SAME-COLOR SURFACE PLASMON-POLARITONS GUIDED BY THE PLANAR INTERFACE OF A METAL AND A SCULPTURED NEMATIC THIN FILM

XUERONG XIAO

Spring 2013

A thesis
submitted in partial fulfillment
of the requirements
for a baccalaureate degree
in Engineering Science
with honors in Engineering Science

Reviewed and approved* by the following:

Akhlesh Lakhtakia
Charles Godfrey Binder Professor in Engineering Science and Mechanics
Thesis Supervisor

Patrick M. Lenahan
Distinguished Professor of Engineering Science and Mechanics
Honors Adviser

Judith A. Todd
P. B. Breneman Deparment Head Chair
Professor, Department of Engineering Science and Mechanics

* Signatures are on file in the Schreyer Honors College and Engineering Science and Mechanics Office.

ABSTRACT

The spin and the orbital angular momentums of multiple surface-plasmon-polariton (SPP) waves guided by a planar interface of a metal and a periodically nonhomogeneous sculptured nematic thin film (SNTF) were theoretically investigated in the canonical boundary-value problem. Both the Minkowski and the Abraham formulations of angular momentums were considered. Multiple SPP waves guided by the metal/SNTF interface in a direction obliquely with respect to the morphologically significant plane of the SNTF were found to have different magnitudes and directions of the spin and the orbital angular momentums. The spin angular momentum is oriented in a variety of directions, but the orbital angular momentum is perpendicular to the direction of propagation and lies in the interface plane. Not only does the periodic nonhomogeneity of the partnering dielectric material engender a multiplicity of SPP waves, but it can also enhance the magnitudes of the spin and orbital components of their angular momentums.

TABLE OF CONTENTS

LIST OF FIGURES

LIST OF TABLES

ACKNOWLEDGEMENTS

I would like to acknowledge my sincere gratitude to Dr. Akhlesh Lakhtakia for giving me the opportunities of doing research in his group. I am deeply indebted for his heuristic and patient guidance on my research, his enlightening lectures on electromagnetics, and his stimulation that always spurred me on. I am also grateful to Dr. Muhammad Faryad for his generous help and invaluable advice on my thesis. I thank Mahmoud Atalla for being so obliging in the discussion on Newton-Raphson method. I thank Weicheng Luo for being such a competitive rival as always. I extend my profuse thanks to my parents for supporting and trusting in me even in the darkest days.

Chapter 1 Introduction

Angular momentum, or moment of momentum, represents the rotational properties of a body about a particular axis. It is defined as the cross product of position vector and linear momentum in classical mechanics. In quantum mechanics, angular momentum is quantized. The classical definition can be applied to quantum mechanics to describe orbital angular momentum. Spin is another type of angular momentum that has no classical counterpart; it is an intrinsic property of particles. The vectorial sum of spin and orbital angular momentum of electromagnetic fields is the total angular momentum. The density of momentum was described in two rival forms recognizing the canonical momentum and the kinetic momentum, proposed by Minkowski (1908) and Abraham (1909) respectively.

Surface-plasmon-polariton waves are excited surface electromagnetic waves that propagate along the interface between a metal and a dielectric material. When the dielectric material is periodically nonhomogeneous, multiple surface-plasmon-polariton waves of the same frequency can be sustained along the interface. It is known that the properties and applications of the surface-plasmonic waves are affected by varying the plasmonic structures. However, the angular momentum of plasmonic phenomena is not thoroughly investigated. The objective of the thesis is to examine the spin and orbital angular momentum, in both Minkowski and Abraham forms, of multiple trains of same-color surface-plasmon-polariton waves independently guided by the planar interface of a metal and a sculptured nematic thin film. The sculptured nematic thin film has a periodically nonhomogeneous anisotropic structure. The results will be compared with the cases in which the partnering dielectric material is (1) homogeneous and isotropic, (2) periodically nonhomogeneous but isotropic, and (3) homogeneous and anisotropic. The theory is modeled by solving the canonical boundary-value problem in which the metal occupies one half-space and the dielectric material the other half. Standard boundary-value conditions are enforced to generate the dispersion relation. Numerical methods are used to solve the problem and compute the time-averaged momentums per unit length. The multiplicity of the plasmonic waves leads to the variations in

the magnitudes and directions of the spin and orbital angular momentums. The flexibility in the design of the sculptured thin film could be applied to the trapping and rotation of single molecule.

The symbols of the physical quantities in this article are listed in Appendix A. It is implicitly assumed that there is no magnetic loss in the dielectric material and that the time-dependence is $\exp(-i\omega t)$. Vectors are in boldface; dyadic are underlined twice; column vectors are boldfaced and enclosed in square brackets, and matrices are underlined twice and square-bracketed.

1.1 Optical Angular Momentum

The rotational characteristics of light beams are expressed by angular momentum of the optical fields. Optical total angular momentum $\boldsymbol{M}$ consists of spin angular momentum $\boldsymbol{M_s}$ and orbital angular momentum $\boldsymbol{M_o}$:

$$\boldsymbol{M} = \boldsymbol{M_s} + \boldsymbol{M_o}. \tag{1}$$

The spin angular momentum (SAM) per photon is equivalent to $\hbar\sigma$, where the integer σ characterizes polarization, and $\sigma \in [-1, 1]$. The orbital angular momentum (OAM) per photon is $l\hbar$ ($l = 0, 1, 2 \ldots$), where l describes the spatial profile of the electromagnetic wave [1]. The first experimental detection and measurement of SAM satisfied the predictions of both field and quantum theories [2]. The well-defined and transferable OAM carried by a Laguerre-Gaussian beam was demonstrated based on the analogy between paraxial optics and quantum mechanics [3]. However, due to the close spacings of the electron energy levels compared to $k_B T$, we do not resort to quantum mechanics here in the description of the optics of metals [4]. Therefore in this thesis, it is desirable to formulate the concepts in classical electromagnetic theory based on Maxwell's equations.

There are two rival expressions for the density of momentum; both are verified experimentally [5], and both have to be considered in the investigation of electromagnetic momentum. The Abraham

momentum density is $\boldsymbol{j}^{Abr} = \boldsymbol{E} \times \boldsymbol{H}/c^2$; the Minkowski momentum density is $\boldsymbol{j}^{Mink} = \boldsymbol{D} \times \boldsymbol{B}$. The time-averaged Abraham angular momentum in a dielectric material can be expressed as

$$\boldsymbol{M}^{Abr} = \frac{\epsilon_0 \mu_o}{2} Re\left[\int \boldsymbol{r} \times (\boldsymbol{E} \times \boldsymbol{H}^*)\, dV\right], \tag{2}$$

and the time-averaged Minkowski angular momentum is

$$\boldsymbol{M}^{Mink} = \frac{\mu_o}{2} Re\left[\int \boldsymbol{r} \times (\boldsymbol{D} \times \boldsymbol{H}^*)\, dV\right]. \tag{3}$$

The time-averaged Abraham spin angular momentum is written as

$$\boldsymbol{M}_s^{Abr} = -\frac{\epsilon_o}{2\omega} Re\left[i \int (\boldsymbol{E}^* \times \boldsymbol{E})\, dV\right], \tag{4}$$

and the time-averaged Minkowski spin angular momentum is

$$\boldsymbol{M}_s^{Mink} = -\frac{1}{2\omega} Re\left[i \int (\boldsymbol{D}^* \times \boldsymbol{E})\, dV\right]. \tag{5}$$

The time-averaged angular momentum per unit length in the two forms, as well as the corresponding spin and orbital components, has been computed and will be presented later in the thesis.

It has been demonstrated that spin and orbital angular momentum are mechanically equivalent [6] and that SAM can be converted to OAM in a nonhomogeneous anisotropic material [7]. The orbital angular momentum can be transferred to trapped particles made of certain material, and the ability to exploit light beams carrying OAM has been one of the key drivers of the study on optical micromanipulation and the design of micromachines. Moreover, OAM can be applied to astrophysics, quantum information encoding and control of atoms [1].

1.2 Multiple Surface-Plasmon-Polariton Waves

When photons are coupled with the collective oscillations of free charges (plasmons) in a metal, surface plasmon-polaritons (SPPs) as the quanta of the excitation are guided and propagate along the planar interface between a metal and a dielectric. The excitation of SPP waves can be achieved using prism

configurations, grating coupler, subwavelength features, waveguides coupler, etc. SPP waves are classically understood in terms of surface electromagnetic waves. The amplitude of a SPP wave decays exponentially into both materials in the directions normal to the interface, and the electromagnetic fields are confined at the near vicinity of the metal/dielectric interface. The confinement enhances the intensity of the fields and thus leads to the high sensitivity of SPP waves to surface conditions.

The unique properties of SPP waves have been utilized in a variety of applications. The enhancement of the fields is widely used in single-molecule detection [8]. The sensitivity is largely exploited in SPP-based devices that are applied to surface analysis such as surface plasmon resonance biosensing [9]. Although SPPs dissipate energy in metal due to absorption, the amplification and lasing with SPPs is made possible by tailoring the plasmonic structures that support the propagation of SPP modes. Along with the flowering of nanofabrication and nanocharacterization techniques, the long-range propagation of SPPs is being studied to make low-loss plasmonic waveguides [10]. The research on the propagation of SPPs aims at the design of plasmonic integrated circuits in which optical information can be carried and processed at nano-scale dimensions. Furthermore, the structures and the constitutive properties of the dielectric material can be artificially engineered to achieve greater complexity, fulfilling the burgeoning demand for advanced materials in nanophotonics research and practical applications [11].

The angular momentum in surface plasmonic phenomena is not completely understood, and the properties and applications depend largely on the engineering of the plasmonic structures. It has been demonstrated that, at the planar interface of a dielectric and a metallic film, light beams that carry OAM can excite surface plasmon modes that also carry OAM [12]. Using a nano-ring plasmonic lens, SPPs exhibit different intensity distribution when excited by photons with different combinations of SAM and OAM. The equivalence and independence of SAM and OAM in the excitation of SPPs are useful for encoding and transmitting information in nanostructures [13]. The conservation of AM has been used to explain excited plasmon modes that emit circularly polarized light from metallic nanowires, which is important for integrated photonics. Also based on the conservation of AM, light carrying OAM can be

used to confine plasmonic fields to metallic nano-spheres, which may contribute to molecular sensing [14]. Helically grooved metal wires with subwavelength-scale corrugation support the propagation of chiral SPPs associated with a helical wave front. The chiral SPPs carry nonzero tunable OAM, which helps the study of light-matter interactions at a subwavelength scale [15]. The plasmonic structure can be carefully engineered so that light-induced rotation does not require any predetermined AM of the incident light. By taking advantage of the enhancement of the EM field due to surface plasmon resonance and the symmetry of the structure, a single nanosized plasmonic motor can drive the rotation of a micrometer-sized silica disk that is 4,000 times larger in volume. The speed and direction of rotation are tunable by changing the illumination wavelength. Such motors can be used for DNA manipulation [16].

At a given frequency, only *p*-polarized SPP wave can be sustained by a metal/dielectric interface, given that the dielectric material is homogeneous. Multiple SPP waves can be excited and propagate along the planar interface of a metal and a periodically nonhomogeneous dielectric material [17]. The partnering dielectric material may be a rugate filter [18], a columnar thin film, a sculptured nematic thin film [19], or a chiral sculptured thin film [20]. Error-free sensing [21], optical sensing of multi-analytes and solar-energy harvesting are possible applications of surface multiplasmonics [22].

Theoretical results have shown that the periodic nonhomogeneity of the dielectric material leads to the multiplicity of the SPP waves. The period has to be greater than a certain value to ensure the multiplicity and the existence of *s*-polarized SPP waves. However, there is a maximum period so that the dielectric is not essentially uniform [19]. The two nonhomogeneous dielectric materials to be examined in this thesis are rugate filter and sculptured nematic thin film (SNTF). A columnar thin film (CTF) is also studied and serves as an important comparison.

Rugate filters are optical coatings with periodically varying refractive index in the direction normal to the film plane [23]. The refractive-index profiles can be controlled depending on the applications. The rugate filter here is chosen to have sinusoidally varying refractive index along the direction perpendicular to the metal/dielectric interface; it is nonhomogeneous but isotropic.

A columnar thin film is a homogeneous and anisotropic material that can be fabricated by oblique angle deposition technique. The shadowing effect ensures that the obliquely incident vapor may not reach certain points on the substrate and that isolated nanocolumns form.

A sculptured nematic thin film is an assembly of parallel nanowires fabricated by rocking the substrate sinusoidally about a fixed axis. The plane perpendicular to the axis is called the morphologically significant plane of SNTF. Physical vapor deposition has been used to grow the thin film, and the relative permittivity profile is sculptured by effectively varying the vapor incident angle sinusoidally about a mean value [21]. The characteristic of the structure has been implemented to design and fabricate rugate filters [24]. It has been documented that multiple SPP waves with the same frequency but different phase speed, attenuation rates, and spatial field profiles can be guided by metal/SNTF interface in the prism-coupled and grating coupled configurations [19, 21, 25-27]. Grounded on the previous work, this thesis is devoted to the enhancement and the wide range of possibilities for the angular momentums that the availability of multiple SPPs waves may offer.

1.3 Potential Societal and Economic Impact

The applications of nanoplasmonics and optical angular momentums mentioned in the previous section encompass advancements in sensing, imaging, micromanipulation, information technologies, computing systems, energy harvesting, and so on. The use of spatial properties of light and the fabrication of nanoplasmonic structures give rise to new devices to detect the orbital angular momentum of light. In addition, DNA damage and gene defects can be sensitively detected; light trapping in solar cells can be improved beyond conventional limit; the possibility of a new generation of compact and superfast computer chips is brought closer. The full exploit of the potential of these fields not only benefits fundamental needs of human beings but also revolutionizes energy supply, computing and communications industry.

Chapter 2 Methodology

2.1 Mathematical Modeling

2.1.1 Canonical Boundary-Value Problem

Canonical boundary-value problem is used to model the propagation of SPP waves. Let z=0 be the planar interface between the metal and the dielectric material. Suppose the half-space z<0 is occupied by an isotropic and homogeneous metal with a complex-valued relative permittivity ϵ_{met}, while the half-space z>0 is occupied by a linear anisotropic and periodically nonhomogeneous dielectric with relative permittivity dyadic $\underline{\underline{\epsilon}}_d(z) = \underline{\underline{\epsilon}}_d(z \pm 2\Omega)$, where 2Ω is the period.

For the analysis below, assume that the SPP wave is launched in the plane x=0. Let the SPP wave propagate in the direction of unit vector $\hat{\boldsymbol{u}}_x$ along the interface z=0 and attenuate as $z \to \pm\infty$. In the region z<0, the wave vector may be written as [19]

$$\boldsymbol{k}_{met} = q\hat{\boldsymbol{u}}_x - \alpha_{met}\hat{\boldsymbol{u}}_z\,, \tag{6}$$

where $q^2 + \alpha_{met}^2 = k_0^2\epsilon_{met}$; q is a complex number, and $Im\,(\alpha_{met}) > 0$ due to the attenuation as $z \to -\infty$. The electric and magnetic field phasors in the metal can be written as

$$\boldsymbol{E}(x,z) = \left[a_p\left(\frac{\alpha_{met}}{k_0}\hat{\boldsymbol{u}}_x + \frac{q}{k_0}\hat{\boldsymbol{u}}_z\right) + a_s\hat{\boldsymbol{u}}_y\right]\exp[i(qx - \alpha_{met}z)]\,, \quad z < 0\,, \tag{7}$$

and

$$\boldsymbol{H}(x,z) = \eta_0^{-1}\left[-a_p\epsilon_{met}\hat{\boldsymbol{u}}_y + a_s\left(\frac{\alpha_{met}}{k_0}\hat{\boldsymbol{u}}_x + \frac{q}{k_0}\hat{\boldsymbol{u}}_z\right)\right]\exp[i(qx - \alpha_{met}z)]\,, \quad z < 0. \tag{8}$$

The unknown scalars a_p and a_s have same units as the electric field, with the subscripts denoting the *p*- and *s*- polarization states with respect to the xz plane respectively.

The electric and magnetic fields in the partnering dielectric material is written as $\boldsymbol{E}(x,z) = \boldsymbol{e}(z)\exp(iqx)$ and $\boldsymbol{H}(x,z) = \boldsymbol{e}(z)\exp(iqx)$. The components $e_z(z)$ and $h_z(z)$ can be expressed in terms of the x and y components of the field phasors composing the column vector

$$[\boldsymbol{f}(z)] = \begin{bmatrix} e_x(z) & e_y(z) & h_x(z) & h_y(z) \end{bmatrix}^T \tag{9}$$

which satisfies the matrix ordinary differential equation

$$\frac{d}{dz}[\boldsymbol{f}(z)] = i\left[\underline{\underline{P}}(z)\right]\cdot[\boldsymbol{f}(z)], \qquad z > 0, \tag{10}$$

where the four-by-four matrix $\left[\underline{\underline{P}}(z)\right]$ depends on q and is a periodic function of z:

$$\left[\underline{\underline{P}}(z \pm 2\Omega)\right] = \left[\underline{\underline{P}}(z)\right]. \tag{11}$$

The relations between the phasor components, as well as the matrix $\left[\underline{\underline{P}}(z)\right]$, are material-specific and will be written in later sections on numerical results for different partnering dielectrics.

Using the Floquet-Lyapunov theorem [28], the solution of the matrix differential equation is found to be of the form

$$[\boldsymbol{f}(z)] = \left[\underline{\underline{F}}(z)\right]\cdot\exp\left\{iz\left[\underline{\underline{\tilde{Q}}}\right]\right\}\cdot[\boldsymbol{f}(0_+)], \tag{12}$$

where

$$\left[\underline{\underline{F}}(z \pm 2\Omega)\right] = \left[\underline{\underline{F}}(z)\right] \tag{13}$$

is a four-by-four matrix with $\left[\underline{\underline{F}}(0)\right]=\left[\underline{\underline{I}}\right]$; $\left[\underline{\underline{\tilde{Q}}}\right]$ is a four-by-four matrix independent of z, and $[\boldsymbol{f}(0_+)]$ is a column four-vector representing the amplitude of fields [17]. The solution Equation (10) lead to the characterization of the optical response in one period of the dielectric material for a specific value of q:

$$[\boldsymbol{f}(2\Omega)] = \left[\underline{\underline{Q}}\right]\cdot[\boldsymbol{f}(0_+)], \tag{14}$$

where the four-by-four matrix $\left[\underline{\underline{Q}}\right]$ is determined using the piecewise-uniform-approximation method [29] as follows. Each period in the z>0 region is divided into a sufficiently large number (N) of minute

spacings, and each spacing is of thickness $2\Omega/N$. The thickness is chosen by ensuring convergent results. For a point in the n[th] spacing, its location on the z-axis is $z_n = 2\Omega\frac{n}{N}$, where $n \in [1, \infty)$. Let $\left[\underline{\underline{W_n}}\right] = \exp\left\{i\frac{2\Omega}{\mathrm{N}}\left[\underline{\underline{P}}(\frac{z_{n-1}+z_n}{2})\right]\right\}$, the matrix $\left[\underline{\underline{Q}}\right]$ can be approximated as [30]

$$\left[\underline{\underline{Q}}\right] \simeq \left[\underline{\underline{W_N}}\right] \cdot \left[\underline{\underline{W_{N-1}}}\right] \cdot \ldots \cdot \left[\underline{\underline{W_2}}\right] \cdot \left[\underline{\underline{W_1}}\right]. \tag{15}$$

Then it is easy to recognize the identity

$$\left[\underline{\underline{Q}}\right] = \exp\left\{i2\Omega\left[\underline{\underline{\tilde{Q}}}\right]\right\}, \tag{16}$$

where $\left[\underline{\underline{Q}}\right]$ and $\left[\underline{\underline{\tilde{Q}}}\right]$ have the same and linearly independent eigenvectors, and their eigenvalues are related. Let $[\boldsymbol{t}]^{(x)}$, with $x \in [1,4]$, be the eigenvector corresponding to the x[th] eigenvalue σ_x of $\left[\underline{\underline{Q}}\right]$; then the corresponding eigenvalue α_x of $\left[\underline{\underline{\tilde{Q}}}\right]$ is given by

$$\alpha_x = -i\frac{\ln\sigma_x}{2\Omega}, \qquad x \in [1,4]. \tag{17}$$

For the propagation of surface waves, the value of q requires that the imaginary parts of α_x are non-zero. The eigenvalues of $\left[\underline{\underline{Q}}\right]$ are labeled such that $Im\left(\alpha_{1,2}\right) > 0$ and $Im\left(\alpha_{3,4}\right) < 0$. Negative imaginary parts of α_x describes amplifying fields as $z \to -\infty$; therefore we eliminate the third and the fourth eigenvalues and set [30]

$$[\boldsymbol{f}(0_+)] = \left[[\boldsymbol{t}]^{(1)} \quad [\boldsymbol{t}]^{(2)}\right] \cdot \begin{bmatrix} b_1 \\ b_2 \end{bmatrix}, \tag{18}$$

where b_1 and b_2 are unknown dimensionless scalars. From Equations (7) and (8), we have

$$[\boldsymbol{f}(0_-)] = \begin{bmatrix} \frac{\alpha_{met}}{k_0} & 0 \\ 0 & 1 \\ 0 & \frac{\alpha_{met}}{k_0\eta_0} \\ -\frac{\epsilon_{met}}{\eta_0} & 0 \end{bmatrix} \cdot \begin{bmatrix} a_p \\ a_s \end{bmatrix}. \tag{19}$$

Standard boundary conditions across the plane z=0 impose continuity requirements on the tangential components of the $\boldsymbol{E}$-field and the $\boldsymbol{H}$-field. Hence we have

$$[\boldsymbol{f}(0_-)] = [\boldsymbol{f}(0_+)], \tag{20}$$

which can be rearranged as the matrix equation

$$\left[\underline{\underline{Y}}\right] \cdot \begin{bmatrix} a_p \\ a_s \\ b_1 \\ b_2 \end{bmatrix} = \begin{bmatrix} 0 \\ 0 \\ 0 \\ 0 \end{bmatrix}. \tag{21}$$

For nontrivial solution, the four-by-four matrix $\left[\underline{\underline{Y}}\right]$ must be singular, leading to the dispersion equation for the SPP wave:

$$\det\left[\underline{\underline{Y}}(q)\right] = 0. \tag{22}$$

This equation is to be solved to determine the wavenumber q.

2.1.2 Abraham and Minkowski Angular Momentums

There are two rival forms of momentum density, as well as two rival forms of angular momentum density. Confining our attention to the xz plane, the time-averaged Abraham angular momentum per unit length along the y-axis can be written based on Equation (2):

$$\begin{aligned} \boldsymbol{M}^{Abr} &= \frac{\epsilon_0 \mu_o}{2} Re\left\{\int_{z=-\infty}^{\infty}\int_{x=0}^{\infty} (x\hat{\boldsymbol{u}}_x + z\hat{\boldsymbol{u}}_z) \times [\boldsymbol{E}(x,z) \times \boldsymbol{H}^*(x,z)]dxdz\right\} \\ &= \frac{\epsilon_0 \mu_o}{4Im(q)} Re\left\{\int_{z=-\infty}^{\infty}\left(\frac{1}{2Im(q)}\,\hat{\boldsymbol{u}}_x + z\hat{\boldsymbol{u}}_z\right) \times [\boldsymbol{e}(z) \times \boldsymbol{h}^*(z)]dz\right\}, \end{aligned} \tag{23}$$

and the time-averaged Minkowski angular momentum per unit length along the y-axis can be written based on Equation (3):

$$\boldsymbol{M}^{Mink} = \frac{\mu_o}{2} Re\left\{\int_{z=-\infty}^{\infty}\int_{x=0}^{\infty} (x\hat{\boldsymbol{u}}_x + z\hat{\boldsymbol{u}}_z) \times [\,\boldsymbol{D}(x,z) \times \boldsymbol{H}^*(x,z)]dxdz\right\}$$

$$= \frac{\mu_o}{4Im(q)} Re\left\{\int_{z=-\infty}^{\infty} \left(\frac{1}{2Im(q)}\, \hat{\boldsymbol{u}}_x + z\hat{\boldsymbol{u}}_z\right) \times [\boldsymbol{d}(z) \times \boldsymbol{h}^*(z)]dz\right\}. \quad (24)$$

The Abraham and the Minkowski momentums are identical in free space but different in materials. The electric displacement field in metal and the partnering dielectric is expressed as

$$\boldsymbol{D}(x,z) = \begin{cases} \epsilon_0 \epsilon_{met} \boldsymbol{E}(x,z), & z < 0 \\ \epsilon_0 \underline{\epsilon}_d(z) \cdot \boldsymbol{E}(x,z), & z > 0 \end{cases}, \quad (25)$$

and $\boldsymbol{d}(z) = \boldsymbol{D}(x,z)\exp(-iqx)$. The time-averaged Abraham angular momentums per unit length in a material, both spin and orbital part, are identical to the ones in free space. The spin part along the y-axis is [31]

$$\boldsymbol{M}_s^{Abr} = -\frac{\epsilon_o}{2\omega} Re\left\{i\int_{z=-\infty}^{\infty}\int_{x=0}^{\infty} [\boldsymbol{E}^*(x,z) \times \boldsymbol{E}(x,z)]dxdz\right\}$$

$$= \frac{\epsilon_0}{4\omega Im(q)} Im\left\{\int_{z=-\infty}^{\infty} [\boldsymbol{e}^*(z) \times \boldsymbol{e}(z)]dz\right\}, \quad (26)$$

and the time-averaged Minkowski angular momentums per unit length along the y-axis is analogously given by [32]

$$\boldsymbol{M}_s^{Mink} = -\frac{1}{2\omega} Re\left\{i\int_{z=-\infty}^{\infty}\int_{x=0}^{\infty} [\boldsymbol{D}^*(x,z) \times \boldsymbol{E}(x,z)]dxdz\right\}$$

$$= \frac{1}{4\omega Im(q)} Im\left\{\int_{z=-\infty}^{\infty} [\boldsymbol{d}^*(z) \times \boldsymbol{e}(z)]dz\right\}. \quad (27)$$

The orbital counterparts are obtained based on Equation (1):

$$\boldsymbol{M}_o^{Abr} = \boldsymbol{M}^{Abr} - \boldsymbol{M}_s^{Abr}, \qquad \boldsymbol{M}_o^{Mink} = \boldsymbol{M}^{Mink} - \boldsymbol{M}_s^{Mink}. \quad (28)$$

The integrations in the metal (over $z \in (-\infty, 0]$) and in the homogeneous isotropic dielectric are not approximated and computed analytically. In the partnering dielectrics that are not homogeneous and isotropic, the open integrals to evaluate in are interpreted as

$$\int_{z=-\infty}^{\infty} [\,\cdot\,]\; dz \simeq \int_{z=-\infty}^{0} [\,\cdot\,]\, dz + \int_{z=0}^{Z} [\,\cdot\,]\, dz. \quad (29)$$

For the integrations over $z \in [0, Z]$, the 32-point Gauss Legendre quadrature is used every 2Ω, as will be elaborated in the next section. For the homogeneous anisotropic material (CTF), Z=2000nm is used for the computation. For the numerical results for periodically nonhomogeneous dielectrics, $Z = 2N_d\Omega$; values of N_d are selected to be $N_d \in [3, 150]$ to ascertain converging results. Since ω is the free space angular frequency of all the SPP waves, and ϵ_0 is an embedded value in Equations (23)-(27), all the values of angular momentums are normalized by a factor of $\frac{\epsilon_0}{\omega}$. For instance,

$$\boldsymbol{m}_s^{Mink} = \frac{\omega}{\epsilon_0}\boldsymbol{M}_s^{Mink}. \tag{30}$$

These normalized quantities carry the units of NmF^{-1}.

2.2 Numerical Methods

The numerical methods used in this work are primarily for root-finding and integration. There are a number of ways to perform the intended computations; specific techniques are designed based on the feasibility and the speed of operation. Newton-Raphson algorithm proved to be robust for root-finding. In terms of integration, since the thickness of the fine segments in the piecewise-uniform-approximation method is on the order of nanometers, even simple methods such as the trapezoidal rule would generate accurate estimates. Simpson's 1/3 Rule had been experimented; the errors were supposedly reduced, but the number and thus the time of computations increased. The method utilized and introduced here is the widespread Gauss-Legendre quadrature which has high-order accuracy and works well with smooth functions. Computer coding for Newton-Raphson method and Gauss-Legendre quadrature is attached in Appendix B.

2.2.1 Numerical Root Finding

Newton-Raphson equation is one of the most commonly used root-locating formulas and is employed to solve Equation (22) for the wavenumber q. The Newton-Raphson method can be derived on the basis of Taylor series. For a general function $g(x)$, an initial guess x_0 is needed to extend a tangent line from the point $[x_0, g(x_0)]$. The point on the x-axis where this tangent crosses is usually an improved estimate of the root. The slope of the first tangent is

$$g'(x_0) = \frac{g(x_0) - 0}{x_0 - x_1}, \tag{31}$$

which can be rearranged to yield

$$x_1 = x_0 - \frac{g(x_0)}{g'(x_0)}. \tag{32}$$

Then the intersection with the x-axis is $(x_1, 0)$. The process is repeated, and every approximation is represented in terms of the previous root, function value, and the slope. The j^{th} estimate is

$$x_{j+1} = x_j - \frac{g(x_j)}{g'(x_j)}, \tag{33}$$

which is called the Newton-Raphson formula. The iteration is stopped until the error is within a certain tolerance.

There is no general convergence criterion for Newton-Raphson. The convergence depends on the nature of the function and the accuracy of the initial guess [33]. Good guesses are usually predicted on the knowledge of physics. In the problem of solving for the wavenumber, the initial guesses are picked around the refractive index of the materials.

2.2.2 Numerical Integration

The general Gaussian integration formulas are good at estimating integrals of the form

$$I = \int_a^b g(x)dx = \int_a^b \rho(x)G(x)dx, \tag{34}$$

where $\rho(x)$ is some weighting function; $g(x)$and $G(x)$ is usually polynomials. Like the Newton-Cotes rules, Gaussian quadrature rules approximate the integral as

$$I \simeq \sum_{t=1}^{n} w_t g(x_t), \tag{35}$$

The difference is that the weights w_t are chosen artfully, and the nodal abscissas x_t are no longer equally spaced. Conventionally, the interval of the integral is from -1 to 1, that is, [a, b] = [-1, 1]. However, any interval can be transformed onto [-1, 1] as follows. Let $x = \frac{1}{2}(b+a) + \frac{1}{2}(b-a)u$, then $dx = \frac{b-a}{2}du$.

$$\int_a^b g(x)dx = \frac{b-a}{2}\int_{-1}^{1} g\left[\frac{1}{2}(b+a) + \frac{1}{2}(b-a)u\right]du$$

$$\simeq \frac{b-a}{2}\sum_{t=1}^{n} w_t g\left[\left(\frac{1}{2}(b+a) + \frac{1}{2}(b-a)x_i\right)\right]. \tag{36}$$

For Gauss-Legendre quadrature, x_t is the tth root of the nth Legendre polynomial $P_n(x)$; the tth weight is given by [34]

$$w_t = \frac{2}{(1-x_t^2)[P_n'(x_t)]^2}. \tag{37}$$

For the integral used in the dielectrics that are not homogeneous and isotropic, Gauss-Legendre quadrature rules are applied with n=32 nodes in the z axis for every 2Ω, the value of which is the period of the periodically nonhomogeneous dielectrics (rugate filter and SNTF). A general formulation for the integrations in the periodic materials may be written as

$$I = \int_{z=0}^{2N_d\Omega} g(z)dz = \sum_{k=1}^{N_d}\int_{z=2(k-1)\Omega}^{2k\Omega} g(z)dz \tag{38}$$

and approximated as

$$I \simeq \sum_{k=1}^{N_d} \left\{ \left[\frac{2k\Omega - 2(k-1)\Omega}{2} \right] \sum_{j=1}^{32} w_j g\left[A_{zj}(k)\right] \right\} = \Omega \sum_{k=1}^{N_d} \sum_{j=1}^{32} w_j g\left[A_{zj}(k)\right], \qquad (39)$$

where $A_{zj}(k) = \frac{1}{2}[2k\Omega + 2(k-1)\Omega] + \frac{1}{2}[2k\Omega - 2(k-1)\Omega]z_j = (2k\Omega - \Omega) + \Omega z_j$. Here z_j is identical to x_t in Equation (37).

Chapter 3 Results and Analyses

The SPP waves propagate along the planar interface between metal and dielectrics. The metal is taken to be homogeneous and isotropic. The four types of partnering dielectric materials compared in this chapter are (1) homogeneous and isotropic, (2) periodically nonhomogeneous and isotropic (rugate filter), (3) homogeneous and anisotropic (CTF), and (4) periodically nonhomogeneous and anisotropic (SNTF). In the following four sections, the polarization states and relative wavenumbers of the SPP waves, integration limits in the positive z direction, and magnitudes and directions of Abraham and Minkowski spin and orbital angular momentums in the three cases will be enumerated or plotted. For all the numerical results presented in this chapter, the free-space wavelength is fixed at $\lambda_0 = 633\ nm$, and the metal is bulk aluminum with relative permittivity $\epsilon_{met} = -56 + 21i$.

3.1 Homogeneous isotropic partnering dielectric material

For the simple case where the partnering dielectric is homogeneous and isotropic, the relative permittivity is $\underline{\underline{\epsilon}}_d = 3.553\underline{\underline{I}}$, where $\underline{\underline{I}}$ is the identity dyadic The value 3.553 is obtained by setting the period of the rugate filter to infinity, as will be shown in the next section. Only one *p*-polarized SPP wave is guided by the interface in this case, meaning the scalar coefficient $a_s = 0V/m$. The coefficient a_p is set to be $1V/m$. The relative wavenumber is given by

$$\frac{q}{k_0} = \sqrt{\frac{\epsilon_{met}\epsilon_d}{\epsilon_{met} + \epsilon_d}} = 1.9394 + 0.0214i. \tag{40}$$

The normalized angular momentums for the single *p*-polarized SPP wave are

$$\boldsymbol{m}_s^{Mink} = -1.37 \times 10^{-11}\widehat{\boldsymbol{u}}_y\ NmF^{-1},\ \ \boldsymbol{m}_o^{Mink} = 8.24 \times 10^{-10}\widehat{\boldsymbol{u}}_y\ NmF^{-1}, \tag{41}$$

and

$$\boldsymbol{m}_s^{Abr} = -9.20 \times 10^{-16} \hat{\boldsymbol{u}}_y \; NmF^{-1}, \;\; \boldsymbol{m}_o^{Abr} = 1.59 \times 10^{-11} \hat{\boldsymbol{u}}_y \; NmF^{-1}, \tag{42}$$

from which we can see that the both the Minkowski and Abraham angular momentums of the SPP wave are entirely in the interface plane and are oriented perpendicular to the direction of propagation. Furthermore, both are predominantly orbital in nature, with the spin and the orbital angular momentums opposing each other. Finally, the Minkowski angular momentums have larger magnitudes than the Abraham counterparts.

3.2 Periodically nonhomogeneous isotropic partnering dielectric material: Rugate Filter

Suppose the rugate filter is periodically nonhomogeneous but isotropic with a relative permittivity dyadic

$$\underline{\underline{\epsilon}}_d(z) = \left[\left(\frac{n_b + n_a}{2}\right) + \left(\frac{n_b - n_a}{2}\right) \sin\left(\pi \frac{z}{\Omega}\right)\right]^2 \underline{\underline{I}}, \qquad z > 0. \tag{43}$$

where n_a and n_b are the lowest and the highest indices of refraction, respectively, and 2Ω is the period. For the numerical results in the section and the next, $\Omega = 200\; nm$ is fixed. The minimum and maximum indices of refraction are also fixed: $n_a = 1.45$ and $n_b = 2.32$. If the period approaches infinity, the dielectric becomes essentially homogeneous with the same relative permittivity in the last section: $\underline{\underline{\epsilon}}_d = \left(\frac{n_b + n_a}{2}\right)^2 \underline{\underline{I}} = 3.553 \underline{\underline{I}}$.

Recall that the components of the electric and magnetic field phasors in the dielectric are interrelated. In the rugate filter, the z components of the phasors are

$$e_z(z) = -\frac{q}{\omega \epsilon_0 \epsilon_d(z)} h_y(z), \qquad z > 0, \tag{44}$$

and

$$h_z(z) = \frac{q}{\omega \mu_0} e_y(z), \qquad z > 0. \tag{45}$$

The material-specific periodic four-by-four matrix $\left[\underline{\underline{P}}(z)\right]$ in the rugate filter is

$$\left[\underline{\underline{P}}(z)\right] = \omega \begin{bmatrix} 0 & 0 & 0 & \mu_0 \\ 0 & 0 & -\mu_0 & 0 \\ 0 & -\epsilon_0\epsilon_d(z) & 0 & 0 \\ \epsilon_0\epsilon_d(z) & 0 & 0 & 0 \end{bmatrix} + \begin{bmatrix} 0 & 0 & 0 & -\mu_0 \\ 0 & 0 & 0 & 0 \\ 0 & \epsilon_0\epsilon_d(z) & 0 & 0 \\ 0 & 0 & 0 & 0 \end{bmatrix}, \quad (46)$$

which composes the matrix differential equation in Equation (10) whose solution leads to the dispersion equation. Five values of the wavenumber q are obtained by solving the dispersion equation. The relative wavenumbers and the corresponding polarization states, as well as the computational results, are listed in Table 1 below.

Table 1 Relative wavenumbers q/k_0 and y components of $\boldsymbol{m}_{s,o}^{Mink,Abr}$ of SPP waves guided by the interface of bulk aluminum and a rugate filter described by Equation (43). The values of N_d used in Equation (29) are provided. The x and z components of $\boldsymbol{m}_{s,o}^{Mink,Abr}$ are identically zero. The computations are performed by setting $\{a_p = 1, a_s = 0\}\, V/m$ for *p*-polarized SPP waves, and $\{a_p = 0, a_s = 1\}\, V/m$ for *s*-polarized SPP waves.

$Pol.$ $States$	q/k_0	N_d	$m_{sy}^{Mink}(N \cdot \frac{m}{F})$	$m_{oy}^{Mink}(N \cdot \frac{m}{F})$	$m_{sy}^{Abr}(N \cdot \frac{m}{F})$	$m_{oy}^{Abr}(N \cdot \frac{m}{F})$
p	$2.1899 + 0.0304i$	3	-1.52×10^{-10}	1.26×10^{-9}	-3.16×10^{-11}	1.91×10^{10}
p	$1.5777 + 0.0055i$	15	-1.26×10^{-9}	1.49×10^{-7}	-5.09×10^{-10}	3.97×10^{-8}
p	$0.9963 + 0.0014i$	150	7.20×10^{-9}	2.05×10^{-5}	7.53×10^{-9}	5.67×10^{-6}
s	$1.9214 + 0.0043i$	5	0	1.58×10^{-9}	0	2.68×10^{-10}
s	$0.9524 + 0.0052i$	40	0	4.40×10^{-9}	0	1.19×10^{-9}

Table 1 shows that five values of wavenumber q are obtained by solving the dispersion equation. The values of the relative wavenumber q/k_0 are listed in Table 1. There are three *p*-polarized and two *s*-polarized SPP waves propagating along the metal/rugate-filter interface. One SPP wave of each linear

polarization state has a phase speed that is higher than the speed of light in the free space, that is, $Re(q/k_0) < 1$. The computed values of $\boldsymbol{m}_{s,o}^{Mink,Abr}$ for the five SPP waves are also provided in Table 1.

For all five SPP waves in Table 1, the x- and z- components of $\boldsymbol{m}_{s,o}^{Mink,Abr}$ are identically zero. Furthermore, the magnitudes of the Minkowski spin and orbital angular momentums are mostly higher than their Abraham counterparts. Finally, the magnitude of the total angular momentum increases significantly as the phase speed $\omega/Re(q)$ increases (i.e., $Re(q)$ decreases), whether the Minkowski or the Abraham formulation is used.

For all three *p*-polarized SPP waves,$\boldsymbol{m}_o$ is larger in magnitude than $\boldsymbol{m}_s$ in both the Minkowski and Abraham formulations. When $Re(q/k_0) > 1$, both the spin and the orbital parts of the angular momentums are anti-parallel, as is the case for the single *p*-polarized SPP wave guided by the interface of bulk aluminum and isotropic and homogeneous dielectric material. An observation of the values of the angular momentums of *p*-polarized SPP waves in Table 1 with those in Equations (41) and (42) shows that the metal/rugate-filter interface can guide SPP waves with an angular momentum being as high as four orders of magnitude higher than that of the SPP wave guided by two homogeneous materials. This comparison is justified because the refractive index of the partnering dielectric material in Section 3.1 is the mean of the minimum and the maximum refractive indices of the partnering dielectric material in this section.

For both *s*-polarized SPP waves in Table 1, $\boldsymbol{m}_s^{Mink}$ and $\boldsymbol{m}_s^{Abr}$ are identically zero. Therefore, in both the Minkowski and Abraham formulations, the angular momentum is completely orbital in nature.

3.3 Homogeneous anisotropic partnering dielectric material: CTF

A columnar thin film (CTF) is a homogeneous, biaxial dielectric material with a relative-permittivity dyadic [35]

$$\underline{\epsilon}_d(z) = \underline{\epsilon}_{CTF}(z) = \underline{S}_z(\gamma) \cdot \underline{s}_y(\chi) \cdot \underline{\epsilon}^{\circ}_{ref} \cdot \underline{s}_y^{-1}(\chi) \cdot \underline{S}_z^{-1}(\gamma), \tag{47}$$

where the dyadics

$$\left.\begin{aligned} \underline{s}_y(\chi) &= (\hat{\boldsymbol{u}}_x\hat{\boldsymbol{u}}_x + \hat{\boldsymbol{u}}_z\hat{\boldsymbol{u}}_z)\cos(\chi) + (\hat{\boldsymbol{u}}_z\hat{\boldsymbol{u}}_x - \hat{\boldsymbol{u}}_x\hat{\boldsymbol{u}}_z)\sin(\chi) + \hat{\boldsymbol{u}}_y\hat{\boldsymbol{u}}_y \\ \underline{\epsilon}^{\circ}_{ref} &= \epsilon_{c1}\hat{\boldsymbol{u}}_z\hat{\boldsymbol{u}}_z + \epsilon_{c2}\hat{\boldsymbol{u}}_x\hat{\boldsymbol{u}}_x + \epsilon_{c3}\hat{\boldsymbol{u}}_y\hat{\boldsymbol{u}}_y \end{aligned}\right\} \tag{48}$$

depend on the inclination angle χ of the columns of CTF. The third dyadic in Equation (47) is stated as

$$\underline{S}_z(\gamma) = \left(\hat{\boldsymbol{u}}_x\hat{\boldsymbol{u}}_x + \hat{\boldsymbol{u}}_y\hat{\boldsymbol{u}}_y\right)\cos\gamma + \left(\hat{\boldsymbol{u}}_y\hat{\boldsymbol{u}}_x - \hat{\boldsymbol{u}}_x\hat{\boldsymbol{u}}_y\right)\sin\gamma + \hat{\boldsymbol{u}}_z\hat{\boldsymbol{u}}_z, \tag{49}$$

so that the morphologically significant plane is formed by the unit vectors $\hat{\boldsymbol{u}}_z$ and $\hat{\boldsymbol{u}}_x\cos\gamma + \hat{\boldsymbol{u}}_y\sin\gamma$, where γ is the angle between the morphologically significant plane and the direction of propagation of the SPP waves.

The z components of the electric and magnetic field phasors in the CTF are

$$\begin{aligned} e_z(z) = {} & \frac{\epsilon_{c4}(\epsilon_{c1} - \epsilon_{c2})\sin(\chi)\cos(\chi)}{\epsilon_{c1}\epsilon_{c2}} e_x(z) \\ & + \kappa\frac{\epsilon_{c4}}{\omega\epsilon_0\epsilon_{c1}\epsilon_{c2}}\left[h_x(z)\sin\gamma - h_y(z)\cos\gamma\right], \qquad z > 0 \end{aligned} \tag{50}$$

where

$$\epsilon_{c4} = \frac{\epsilon_{c1}\epsilon_{c2}}{\epsilon_{c1}\cos^2(\chi) + \epsilon_{c2}\sin^2(\chi)}, \tag{51}$$

and

$$h_z(z) = -\frac{q}{\omega\mu_0}\left[e_x(z)\sin\gamma - e_y(z)\cos\gamma\right]. \qquad z > 0 \tag{52}$$

The material-specific periodic four-by-four matrix $\left[\underline{P}(z)\right]$ in the CTF is

$$\left[\underline{\underline{P}}(z)\right] = \omega \begin{bmatrix} 0 & 0 & 0 & \mu_0 \\ 0 & 0 & -\mu_0 & 0 \\ 0 & -\epsilon_0\epsilon_{c3} & 0 & 0 \\ \epsilon_0\epsilon_{c4} & 0 & 0 & 0 \end{bmatrix}$$

$$+ q\frac{\epsilon_{c4}(\epsilon_{c1}-\epsilon_{c2})}{\epsilon_{c1}\epsilon_{c2}}\sin(\chi)\cos(\chi)\begin{bmatrix} \cos\gamma & 0 & 0 & 0 \\ \sin\gamma & 0 & 0 & 0 \\ 0 & 0 & 0 & 0 \\ 0 & 0 & -\sin\gamma & \cos\gamma \end{bmatrix}$$

$$+ \frac{q^2}{\omega\epsilon_0}\frac{\epsilon_{c4}}{\epsilon_{c1}\epsilon_{c2}}\begin{bmatrix} 0 & 0 & \cos\gamma\sin\gamma & -\cos^2\gamma \\ 0 & 0 & \sin^2\gamma & -\cos\gamma\sin\gamma \\ 0 & 0 & 0 & 0 \\ 0 & 0 & 0 & 0 \end{bmatrix}$$

$$+ \frac{q^2}{\omega\mu_0}\begin{bmatrix} 0 & 0 & 0 & 0 \\ 0 & 0 & 0 & 0 \\ -\cos\gamma\sin\gamma & \cos^2\gamma & 0 & 0 \\ -\sin^2\gamma & \cos\gamma\sin\gamma & 0 & 0 \end{bmatrix}, \tag{53}$$

which is not a functions of z.

An CTF made of titanium oxide [37] is considered, with

$$\left.\begin{aligned} \epsilon_{c1} &= [1.0443 + 2.7394v - 1.3697v^2]^2 \\ \epsilon_{c2} &= [1.6765 + 1.5649v - 0.7825v^2]^2 \\ \epsilon_{c3} &= [1.3586 + 2.1109v - 1.0554v^2]^2 \\ \chi &= \tan^{-1}[2.8818\tan\chi_{\mathrm{v}}] \end{aligned}\right\}, \tag{54}$$

where $v = 2\chi_{\mathrm{v}}/\pi$, and $\chi_v = 45°$for all numerical results presented here for a comparison with the ones for a metal/SNTF interface provided in Section 3.4.

Only one SPP wave can be guided by the metal/CTF interface irrespective of the angle γ. The real and imaginary parts of the relative wavenumbers q/k_0 obtained by the solution of the dispersion equation (22) are provided in Figure 1 below as functions of $\gamma \in [0°, 90°]$. The SPP wave is neither *p*- nor *s*-polarized except when $\gamma = 0°$.

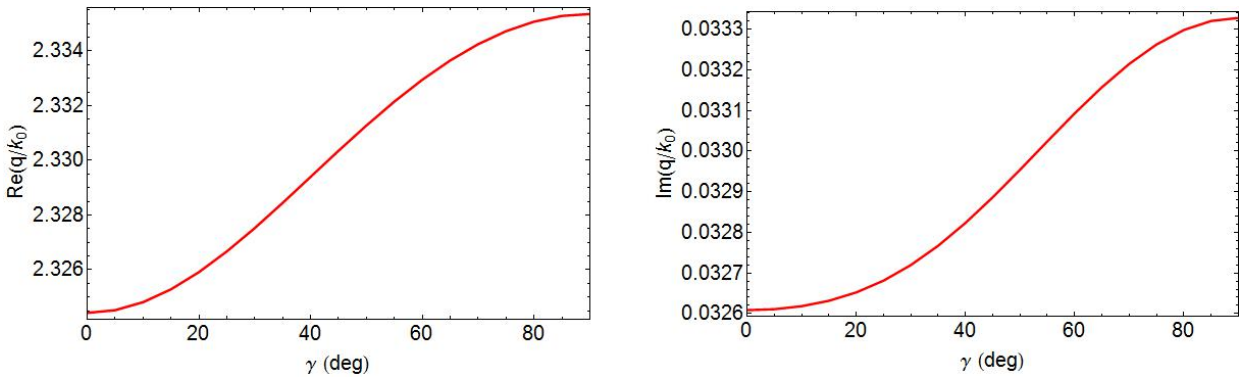

Figure 1 The real and imaginary parts of relative wavenumbers q/k_0 as functions of γ for SPP waves guided by a metal/CTF interface. The metal is bulk aluminum whereas the chosen CTF is described in Section 3.3.

3.3.1 $\gamma = 0°$

When $\gamma = 0°$, the SPP wave is *p*-polarized, with $q/k_0 = 2.3244 + 0.03261i$. for this SPP wave, we found that

$$\boldsymbol{m}_s^{Mink} = -1.48 \times 10^{-10}\hat{\boldsymbol{u}}_y \, NmF^{-1}, \;\; \boldsymbol{m}_o^{Mink} = 1.83 \times 10^{-9}\hat{\boldsymbol{u}}_y \, NmF^{-1}, \tag{55}$$

and

$$\boldsymbol{m}_s^{Abr} = -2.91 \times 10^{-11}\hat{\boldsymbol{u}}_y \, NmF^{-1}, \;\; \boldsymbol{m}_o^{Abr} = 2.27 \times 10^{-10}\hat{\boldsymbol{u}}_y \, NmF^{-1}, \tag{56}$$

with $a_p = 1 \, V/m$ and $a_s = 0$. As was the case with isotropic partnering dielectric materials in Sections 3.1 and 3.2, the angular momentum of the SPP wave lies entirely in the interface plane and is oriented perpendicular to the direction of the propagation, in both the Minkowski and Abraham formulations. Furthermore, in both formulations, with a small spin part opposing a large orbital part, the angular momentum is predominantly orbital in nature. In addition, $\left|\boldsymbol{m}_s^{Mink}\right| > |\boldsymbol{m}_s^{Abr}|$, and $\left|\boldsymbol{m}_o^{Mink}\right| > |\boldsymbol{m}_o^{Abr}|$ by an order of magnitude.

3.3.2 $\gamma \in (0°, 90°]$

For $\gamma \in (0°, 90°]$, the Cartesian components of $\boldsymbol{m}_{s,o}^{Mink,Abr}$ are plotted in Figure 2 below for sole SPP wave guided by the metal/CTF interface. All Cartesian components of $\boldsymbol{m}_{s,o}^{Mink,Abr}$ are non-zero. Furthermore, the Cartesian components of the spin angular momentum are smaller than their orbital counterparts in both the Minkowski and Abraham formulations.

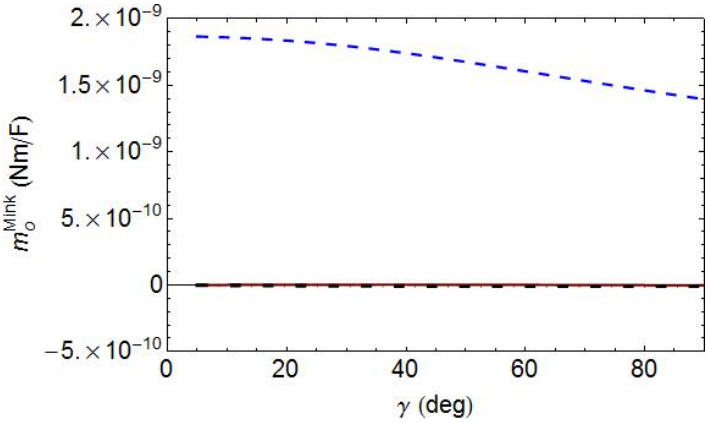

(a) Orbital - Minkowski

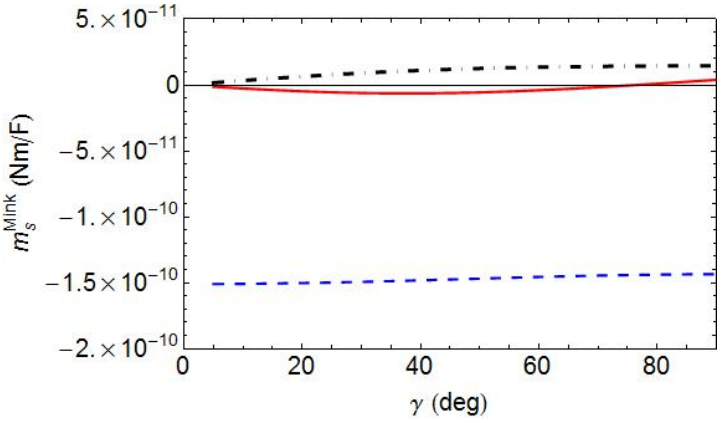

(b) Spin - Minkowski

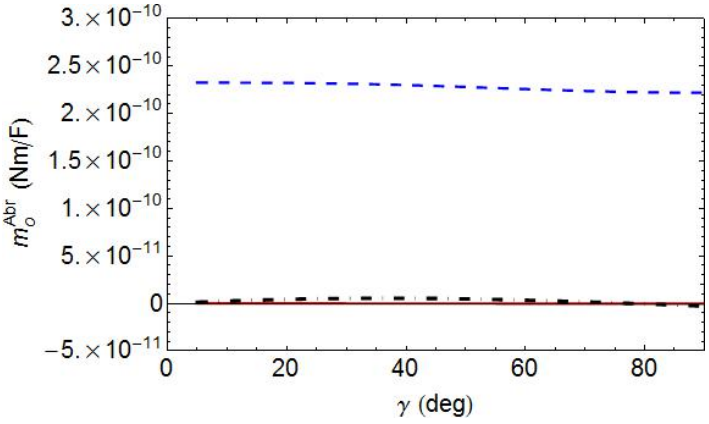

(c) Orbital - Abraham

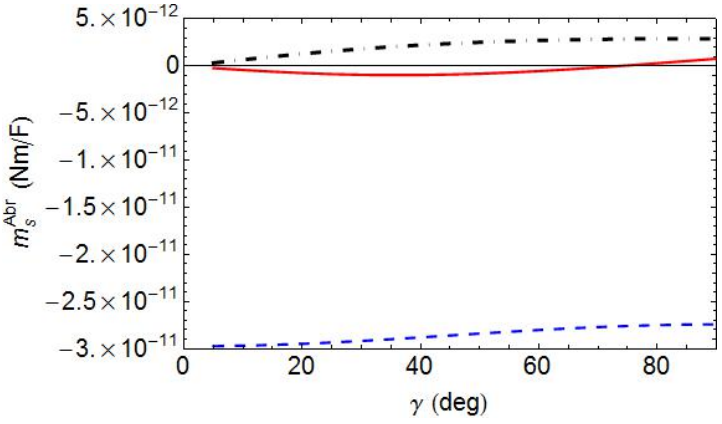

(d) Spin - Abraham

Figure 2 The Cartesian components of (a) $\boldsymbol{m}_o^{Mink}$, (b) $\boldsymbol{m}_s^{Mink}$, (c) $\boldsymbol{m}_o^{Abr}$, and (4) $\boldsymbol{m}_s^{Abr}$ as functions of γ for SPP waves guided by the interface of bulk aluminum and the chosen titanium-oxide CTF, when $a_p = 1V/m$. The x-, y-, and z-directed components are represented by solid red, blue dashed, and black chain-dashed lines, respectively. For computations, $N_d = 3$ is set after ascertaining that the values of the Cartesian components of the angular momentums are converged.

A scan of Figure 2(a) shows that the magnitude of the y-directed component of $\boldsymbol{m}_o^{Mink}$ is significantly larger than the magnitudes of its x- and z- directed components; therefore, $\boldsymbol{m}_o^{Mink}$ is predominantly directed along an axis (y axis) that lies wholly in the interface plane and is oriented perpendicular to the direction of propagation. Similarly, a scan of Figures 2(c) shows that $\boldsymbol{m}_o^{Abr}$ is also oriented very similarly. But, $\boldsymbol{m}_s^{Mink}$ and $\boldsymbol{m}_s^{Abr}$ in Figure 2(c) and (d), respectively, are oriented along the -y axis.

A comparison of Figures 2(a, b) with 2(c, d) shows that the magnitudes of the Cartesian components of the Minkowski orbital and spin angular momentums generally exceed those of their Abraham counterparts.

The magnitudes of $\boldsymbol{m}_{s,o}^{Mink,Abr}$ as functions of $\gamma \in (0°, 90°]$ are presented in Figure 3 below. The spin angular momentum is weaker than the orbital angular momentum, in both the Minkowski and Abraham formulations. Furthermore, $\left|\boldsymbol{m}_s^{Mink}\right| > |\boldsymbol{m}_s^{Abr}|$, and $\left|\boldsymbol{m}_o^{Mink}\right| > |\boldsymbol{m}_o^{Abr}|$.

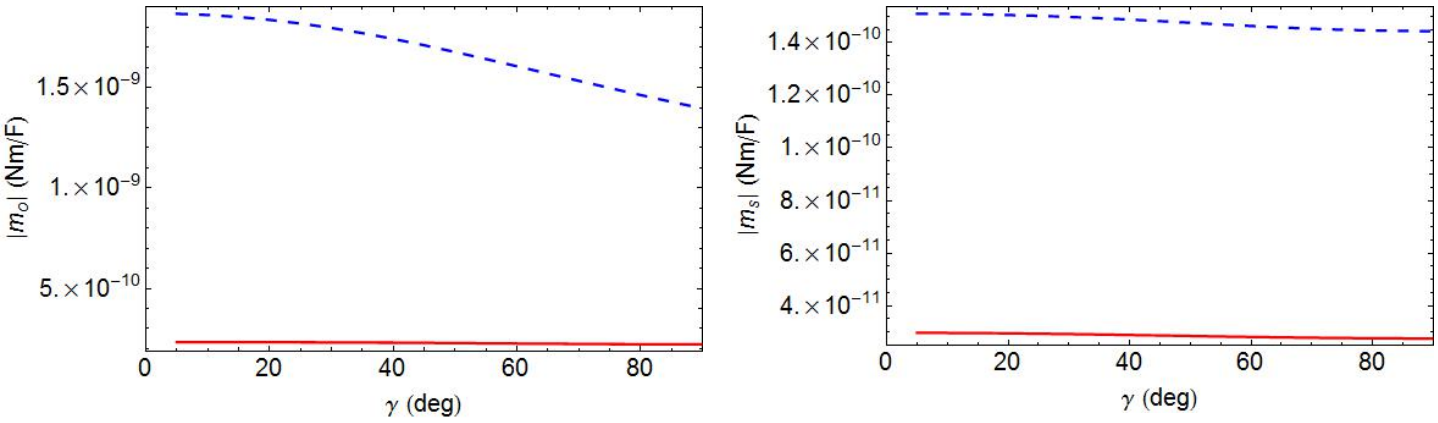

(a) (b)

Figure 3 The magnitudes of $\boldsymbol{m}_{s,o}^{Mink,Abr}$ as functions of γ for SPP waves guided by the interface of bulk aluminum and the chosen titanium-oxide CTF, when $a_p = 1V/m$. Results for the Abraham and Minkowski formulations are denoted by solid red and blue-chain dashed lines, respectively. For computations, $N_d = 3$ is set after ascertaining that the values of the Cartesian components of the angular momentums are converged.

3.4 Periodically nonhomogeneous anisotropic partnering dielectric material: SNTF

In the case where the half-space z>0 is occupied by an SNTF that is periodically nonhomogeneous and isotropic, the relative-permittivity dyadic is

$$\underline{\underline{\epsilon}}_d(z) = \underline{\underline{\epsilon}}_{SNTF}(z) = \underline{\underline{S}}_z(\gamma) \cdot \underline{\underline{S}}_y(z) \cdot \underline{\underline{\epsilon}}^{\circ}_{ref}(z) \cdot \underline{\underline{S}}_y^{-1}(z) \cdot \underline{\underline{S}}_z^{-1}(\gamma), \tag{57}$$

where the dyadics

$$\left.\begin{aligned} \underline{\underline{S}}_y(z) &= (\hat{\boldsymbol{u}}_x\hat{\boldsymbol{u}}_x + \hat{\boldsymbol{u}}_z\hat{\boldsymbol{u}}_z)\cos[\chi(z)] + (\hat{\boldsymbol{u}}_z\hat{\boldsymbol{u}}_x - \hat{\boldsymbol{u}}_x\hat{\boldsymbol{u}}_z)\sin[\chi(z)] + \hat{\boldsymbol{u}}_y\hat{\boldsymbol{u}}_y \\ \underline{\underline{\epsilon}}^{\circ}_{ref}(z) &= \epsilon_{s1}(z)\hat{\boldsymbol{u}}_z\hat{\boldsymbol{u}}_z + \epsilon_{s2}(z)\hat{\boldsymbol{u}}_x\hat{\boldsymbol{u}}_x + \epsilon_{s3}(z)\hat{\boldsymbol{u}}_y\hat{\boldsymbol{u}}_y \end{aligned}\right\} \tag{58}$$

depend on the vapor incident angle $\chi_v(z) = \tilde{\chi}_v + \delta_v \sin(\pi z/\Omega)$ that varies sinusoidally with period 2Ω. The third dyadic on the right side of Equation (57) is given by Equation (49), the morphologically significant plane of the SNTF is also formed by the unit vector $\hat{\boldsymbol{u}}_z$ and $\hat{\boldsymbol{u}}_x \cos\gamma + \hat{\boldsymbol{u}}_y \sin\gamma$. The quantities $\epsilon_{s1}(z')$, $\epsilon_{s2}(z')$, and $\epsilon_{s3}(z')$ are the eigenvalues of $\underline{\underline{\epsilon}}^{o}_{ref}(z')$ – and hence of $\underline{\underline{\epsilon}}_{SNTF}(z')$ – and should be interpreted as the principal relative-permittivity scalars in the plane $z = z'$ [36],whereas $\chi(z')$ is the inclination angle of the columnar morphology with respect to the same plane. These four quantities depend on $\chi_v(z')$, the conditions for the fabrication of the SNTF, and the material(s) evaporate to fabricate the SNTF [19].

The z components of the electric and magnetic field phasors in the SNTF are

$$e_z(z) = \frac{\epsilon_{s4}(z)[\epsilon_{s1}(z) - \epsilon_{s2}(z)]\sin[\chi(z)]\cos[\chi(z)]}{\epsilon_{s1}(z)\epsilon_{s2}(z)} e_x(z) + \kappa \frac{\epsilon_{s4}(z)}{\omega\epsilon_0\epsilon_{s1}(z)\epsilon_{s2}(z)} \left[h_x(z)\sin\gamma - h_y(z)\cos\gamma\right], \quad z > 0 \tag{59}$$

where

$$\epsilon_{s4}(z) = \frac{\epsilon_{s1}(z)\epsilon_{s2}(z)}{\epsilon_{s1}(z)\cos^2[\chi(z)] + \epsilon_{s2}(z)\sin^2[\chi(z)]}, \tag{60}$$

and

$$h_z(z) = -\frac{q}{\omega\mu_0}\left[e_x(z)\sin\gamma - e_y(z)\cos\gamma\right]. \qquad z > 0 \tag{61}$$

The material-specific periodic four-by-four matrix $\left[\underline{\underline{P}}(z)\right]$ in the SNTF is

$$\left[\underline{\underline{P}}(z)\right] = \omega \begin{bmatrix} 0 & 0 & 0 & \mu_0 \\ 0 & 0 & -\mu_0 & 0 \\ 0 & -\epsilon_0\epsilon_{s3}(z) & 0 & 0 \\ \epsilon_0\epsilon_{s4}(z) & 0 & 0 & 0 \end{bmatrix}$$

$$+ q\frac{\epsilon_{s4}(z)[\epsilon_{s1}(z)-\epsilon_{s2}(z)]}{\epsilon_{s1}(z)\epsilon_{s2}(z)}\sin[\chi(z)]\cos[\chi(z)]\begin{bmatrix} \cos\gamma & 0 & 0 & 0 \\ \sin\gamma & 0 & 0 & 0 \\ 0 & 0 & 0 & 0 \\ 0 & 0 & -\sin\gamma & \cos\gamma \end{bmatrix}$$

$$+ \frac{q^2}{\omega\epsilon_0}\frac{\epsilon_{s4}(z)}{\epsilon_{s1}(z)\epsilon_{s2}(z)}\begin{bmatrix} 0 & 0 & \cos\gamma\sin\gamma & -\cos^2\gamma \\ 0 & 0 & \sin^2\gamma & -\cos\gamma\sin\gamma \\ 0 & 0 & 0 & 0 \\ 0 & 0 & 0 & 0 \end{bmatrix}$$

$$+ \frac{q^2}{\omega\mu_0}\begin{bmatrix} 0 & 0 & 0 & 0 \\ 0 & 0 & 0 & 0 \\ -\cos\gamma\sin\gamma & \cos^2\gamma & 0 & 0 \\ -\sin^2\gamma & \cos\gamma\sin\gamma & 0 & 0 \end{bmatrix}. \tag{62}$$

An SNTF made of titanium oxide [37] is considered, with

$$\left.\begin{aligned} \epsilon_{s1}(z) &= [1.0443 + 2.7394v(z) - 1.3697v^2(z)]^2 \\ \epsilon_{s2}(z) &= [1.6765 + 1.5649v(z) - 0.7825v^2(z)]^2 \\ \epsilon_{s3}(z) &= [1.3586 + 2.1109v(z) - 1.0554v^2(z)]^2 \\ \chi(z) &= \tan^{-1}[2.8818\tan\chi_{\mathrm{v}}(z)] \end{aligned}\right\} \tag{63}$$

where $v(z) = 2\chi_{\mathrm{v}}(\mathrm{z})/\pi$, $\tilde{\chi}_v = 45^\circ$, and $\delta_v = 30^\circ$ for all numerical results presented here. Let us note that the CTF considered in Section 3.3 can be treated as a special case of the SNTF considered in this section with $\delta_v = 0^\circ$.

The real and imaginary parts of the relative wavenumbers q/k_0 obtained by the solution of the dispersion equation (22) as functions of γ are provided in Figure 4, reproduced from Ref. [19]. Either two or three SPP waves can be guided by the metal/SNTF interface depending on the angle γ between the direction of propagation and the morphologically significant plane of the SNTF. The SPP waves guided by the metal/SNTF interface have hybridized polarization states, except for the case where $\gamma = 0^\circ$, at which the SNTF is essentially an isotropic rugate filter and has linear polarization states.

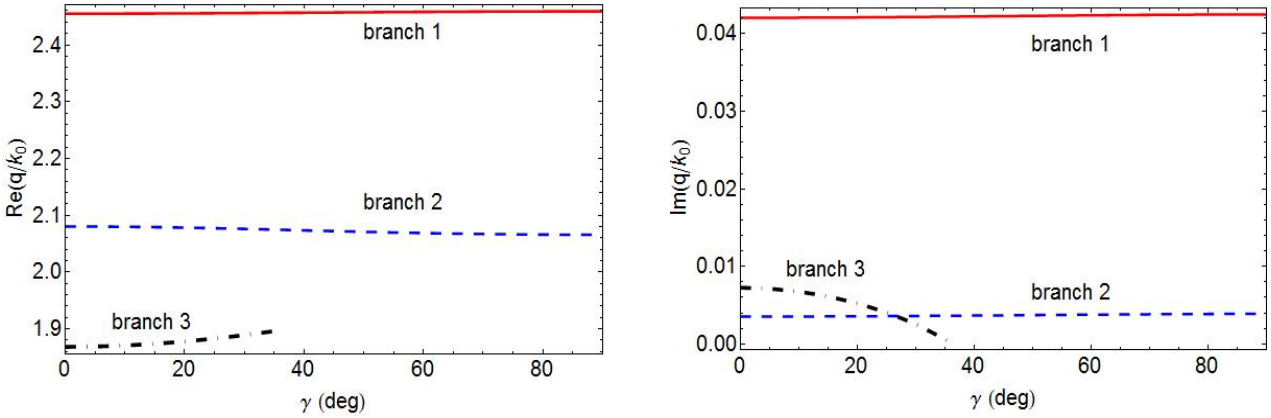

Figure 4 The real and imaginary parts of relative wavenumbers q/k_0 as functions of γ for SPP wave guided by metal/SNTF interface. The metal is bulk aluminum whereas the chosen SNTF is described in Section 3.4.

3.4.1 $\gamma = 0°$

When $\gamma = 0°$, two *p*- and one *s*-polarized SPP waves are guided by the metal/SNTF interface. The computational results of relative wavenumbers and the y components of $\boldsymbol{m}_{s,o}^{Mink,Abr}$ are listed in Table 2 below.

Table 2 Relative wavenumbers q/k_0 and y components of $\boldsymbol{m}_{s,o}^{Mink,Abr}$ of SPP waves guided by the interface of bulk aluminum and the chosen titanium oxide SNTF when $\gamma = 0°$. The values of N_d used in Equation (29) are provided. The x and z components of $\boldsymbol{m}_{s,o}^{Mink,Abr}$ are identically zero. The computations are performed by setting $\{a_p = 1, a_s = 0\}\, V/m$ for *p*-polarized SPP waves, and $\{a_p = 0, a_s = 1\}\, V/m$ for *s*-polarized SPP waves.

$Pol.$ $States$	q/k_0	N_d	$m_{sy}^{Mink}(N\cdot\frac{m}{F})$	$m_{oy}^{Mink}(N\cdot\frac{m}{F})$	$m_{sy}^{Abr}(N\cdot\frac{m}{F})$	$m_{oy}^{Abr}(N\cdot\frac{m}{F})$
$p(Branch1)$	$2.4550+0.0421i$	2	-1.06×10^{-10}	8.10×10^{-10}	-1.83×10^{-11}	9.89×10^{-11}
$s(Branch2)$	$2.080+0.0035i$	6	0	2.73×10^{-9}	0	4.29×10^{-10}
$p(Branch3)$	$1.8683+0.0073i$	10	-8.49×10^{-10}	1.58×10^{-7}	-2.51×10^{-10}	2.02×10^{-8}

For both *p*-polarized SPP waves, spin and orbital angular momentums are anti-parallel in both the Minkowski and Abraham formulations. Furthermore, both parts of the angular momentum are directed along an axis that lies in the interface plane and is oriented perpendicular to the direction of propagation—in accord with a *p*-polarized SPP wave guided by either a metal/isotropic-dielectric or a metal/CTF interface when $Re\{q/k_0\}>1$. For the *s*-polarized SPP wave, spin is identically zero in both the Minkowski and Abraham formulations.

As are the cases for the interface of a metal and an isotropic dielectric partnering material—whether homogeneous or periodically nonhomogeneous—the magnitudes of the Minkowski spin and orbital angular momentums are higher than those of their Abraham counterparts. Also, the magnitudes of $\boldsymbol{m}_{s,o}^{Mink,Abr}$ increase significantly as the phase speed $\omega/Re\{q\}$ of the SPP wave increases.

3.4.2 $\boldsymbol{\gamma\in(0^\circ,90^\circ]}$

When $\gamma\in(0^\circ,90^\circ]$, the Catesian components of $\boldsymbol{m}_{s,o}^{Mink,Abr}$ are plotted in Figure 5 below for the SPP waves guided by the metal/SNTF interface for the solutions on Branch 1 in Figure 4. The y-directed component of $\boldsymbol{m}_o^{Mink}$ is greater in magnitude than the other components of $\boldsymbol{m}_o^{Mink}$. Therefore, $\boldsymbol{m}_o^{Mink}$ can be said to lie in the interface plane and oriented perpendicular to the direction of propagation. A similar

remark can also be made for $\boldsymbol{m}_s^{Mink}$, $\boldsymbol{m}_o^{Abr}$, and $\boldsymbol{m}_s^{Abr}$, although the spin is directed opposite to the orbital angular momentum. A comparison of Figure 5 and 2 shows that the angular momentum of the SPP wave represented by Branch 1 in Figure 4 for the metal/SNTF interface and for the sole SPP wave guided by the metal/CTF interface are similar in magnitudes and directions, in both formulations.

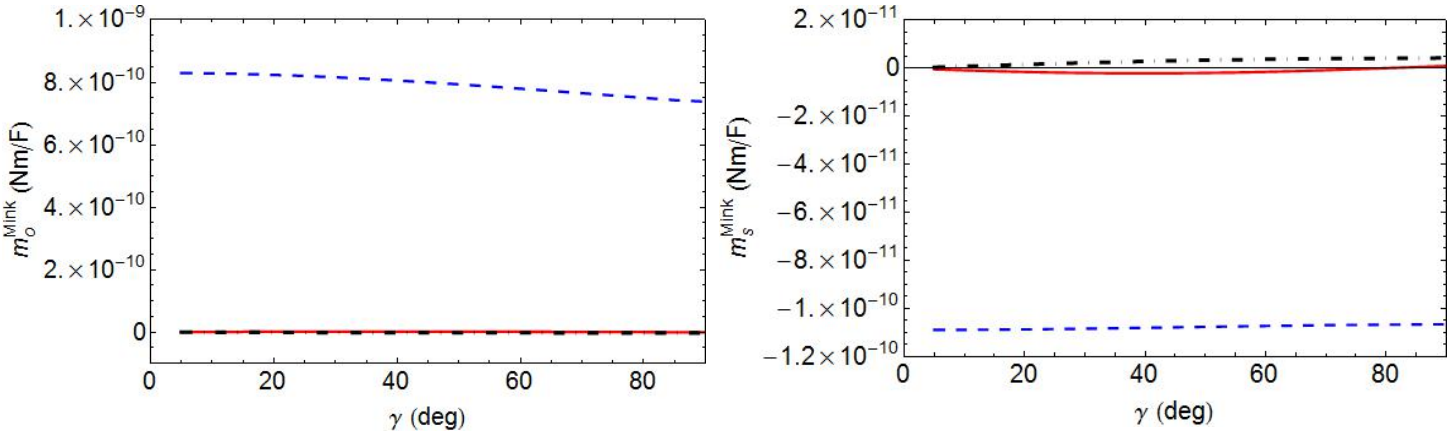

(a) Orbital - Minkowski

(b) Spin - Minkowski

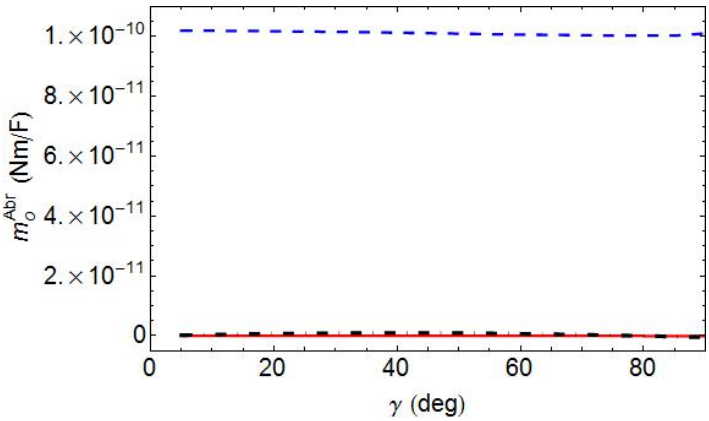

(c) Orbital - Abraham

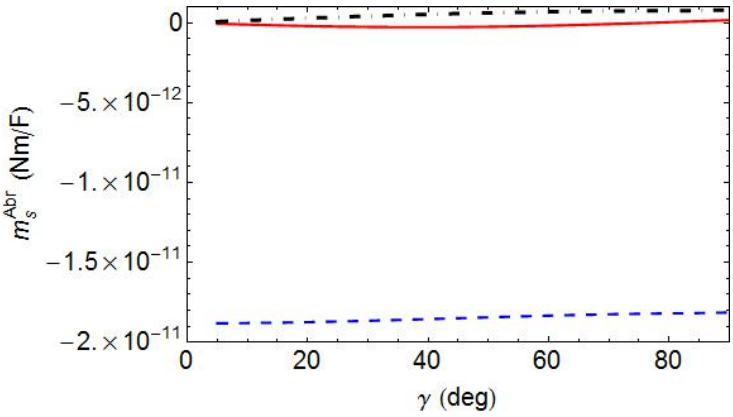

(d) Spin - Abraham

Figure 5 The Cartesian components of (a) $\boldsymbol{m}_o^{Mink}$, (b) $\boldsymbol{m}_s^{Mink}$, (c) $\boldsymbol{m}_o^{Abr}$, and (4) $\boldsymbol{m}_s^{Abr}$ as functions of γ for solution Branch 1 (in Figure 4) representing the SPP waves guided by the interface of bulk aluminum and the chosen titanium-oxide SNTF, when $a_p = 1V/m$. The x-, y-, and z-directed components are

represented by solid red, blue dashed, and black chain-dashed lines, respectively. For computations, $N_d = 2$ is set after ascertaining that the values of the Cartesian components of the angular momentums are converged.

For the SPP waves on Branch 2, the Cartesian components of $\boldsymbol{m}_{s,o}^{Mink,Abr}$ are plotted in Figure 6 below as functions of γ. A scan of Figures 6(a, c) shows that the orbital angular momentum lies almost completely in the interface plane and is perpendicular to the direction of propagation. However, $\boldsymbol{m}_s^{Mink}$ lies in the xz plane because the x- and z- directed components of $\boldsymbol{m}_s^{Mink}$ are similar in magnitude and are greater in magnitude than the y-directed component [Figure 6(b)]. Similarly, $\boldsymbol{m}_s^{Abr}$ also lies in the xz plane. A comparison of Figures 5 and 6 shows that the Cartesian components of the angular momentums of SPP waves on Branch 2 are significantly larger than those on Branch 1.

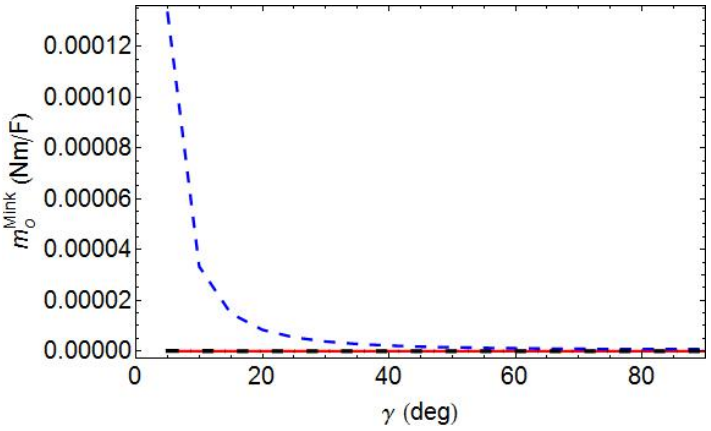

(a) Orbital - Minkowski

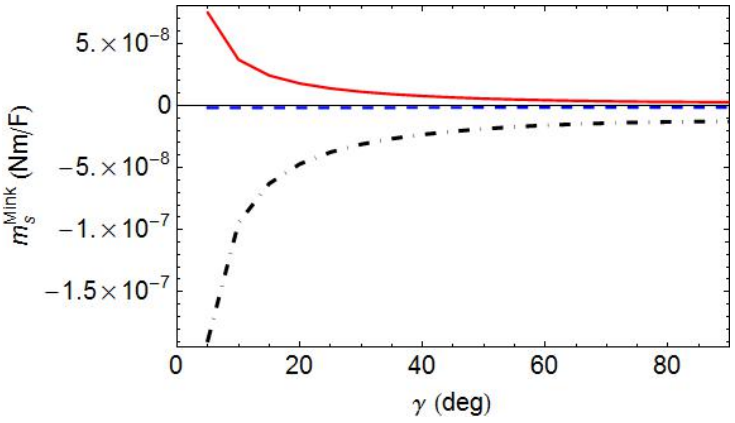

(b) Spin - Minkowski

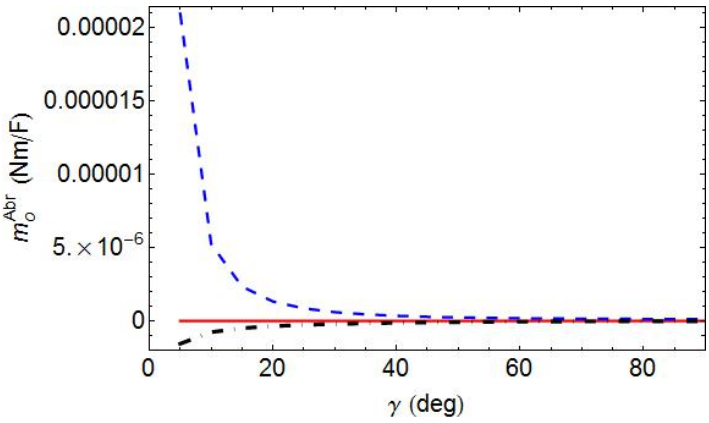

(c) Orbital - Abraham

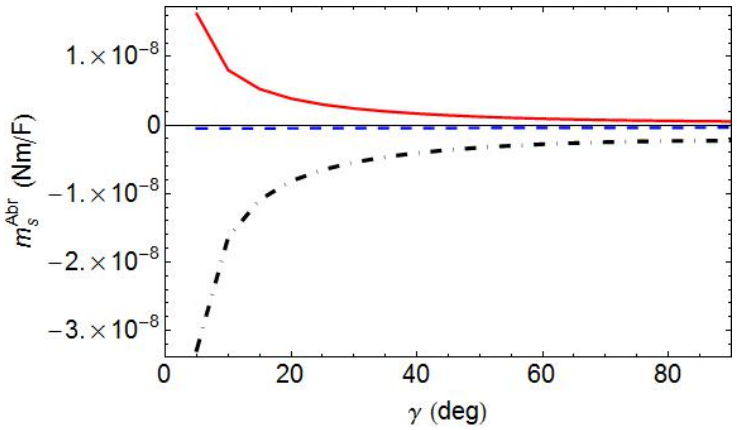

(d) Spin - Abraham

Figure 6 Same as Figure 5 except that this is for solution Branch 2 and that $N_d = 6$.

The Cartesian components of $\boldsymbol{m}_{s,o}^{Mink,Abr}$ for Branch 3 are presented only for $\gamma \leq 30°$ in Figure 7 below, for convenience, since the magnitude of either one or two components increases rapidly as γ increases beyond $30°$ to $36°$. Figures 7(a) and (c) show that the orbital angular momentum is directed perpendicular to the direction of propagation and lies in the interface plane, because the y-directed component is larger in magnitude than the x- and z-directed components, in both formulations. Similarly, Figure 7(b) and (d) show that $\boldsymbol{m}_s^{Mink}$ and $\boldsymbol{m}_s^{Abr}$ are directed along the –y direction when γ is small and lies in the yz plane when γ is large.

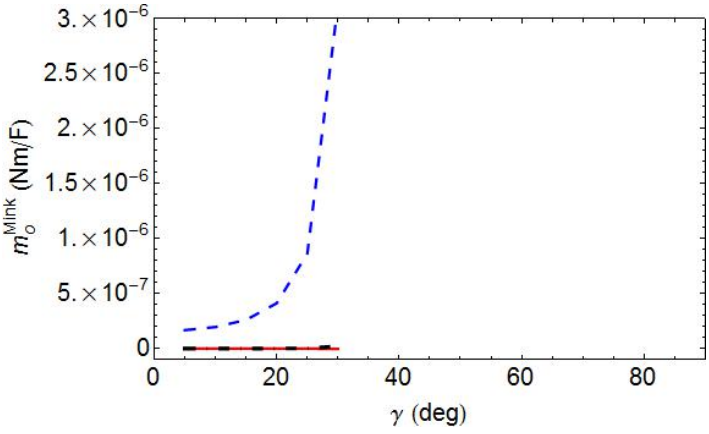

(a) Orbital - Minkowski

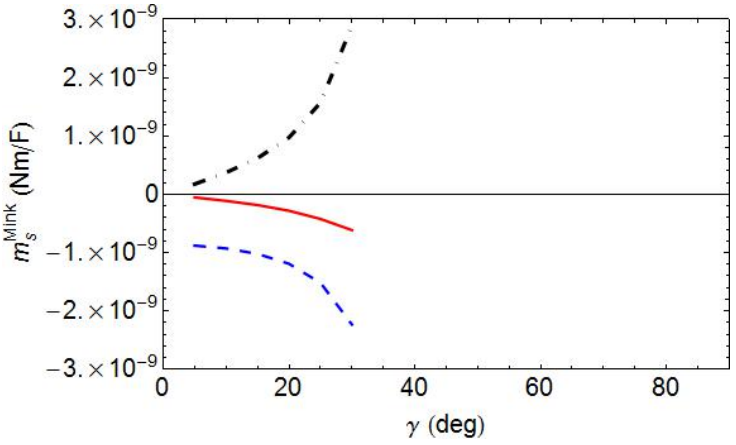

(b) Spin - Minkowski

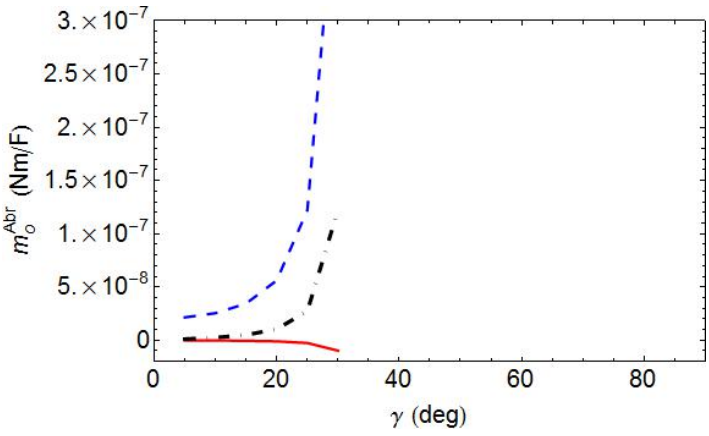

(c) Orbital - Abraham

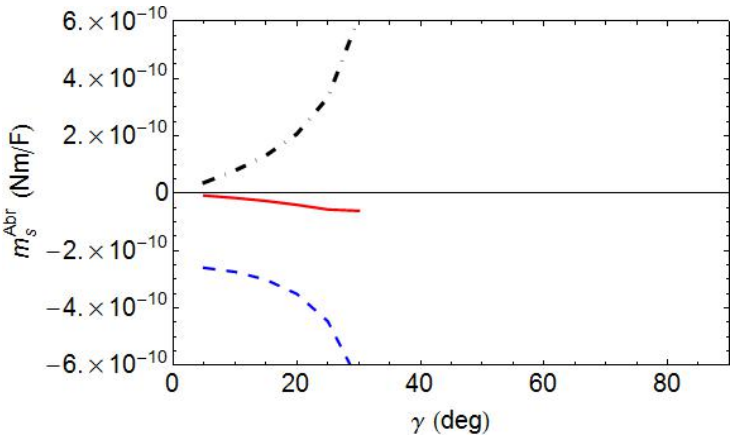

(d) Spin - Abraham

Figure 7 Same as Figure 5 except that this is for solution Branch 3 and that $N_d = 10$.

From Figures 5-7, we conclude that all Cartesian components of Minkowski angular momentums are non-zero for $\gamma \in (0°, 90°]$, in contrast to the case when $\gamma = 0°$. The non-zero x- and z- directed components are also in contrast with the results presented in Sections 3.1 and 3.2.

The magnitudes of $\boldsymbol{m}_{s,o}^{Mink,Abr}$ as functions of $\gamma \in (0°, 90°]$ are presented in Figure 8 for all three branches of solutions in Figure 4. A quick scan of Figure 8 shows the availability of a wide range of magnitudes of $\boldsymbol{m}_s$ and $\boldsymbol{m}_o$, in both the Minkowski and Abraham formulations, for different SPP waves

guided by the metal/SNTF interface. A comparison of Figures 8(a, c, d) and (b, d, f) indicates that the magnitude of the spin angular momentum is lower than that of the orbital angular momentum in both formulations. Moreover, the Minkowski orbital and spin angular momentums are larger in magnitude than their Abraham counterparts. These trends are similar to the cases when partnering dielectric material is isotropic, or homogeneous and anisotropic.

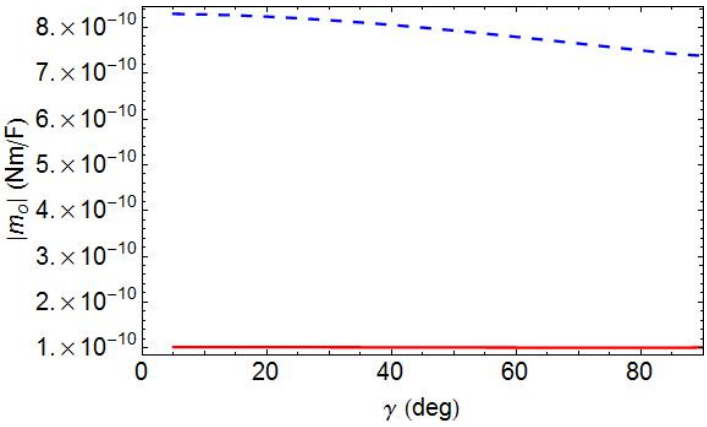

(a) Orbital – Branch 1

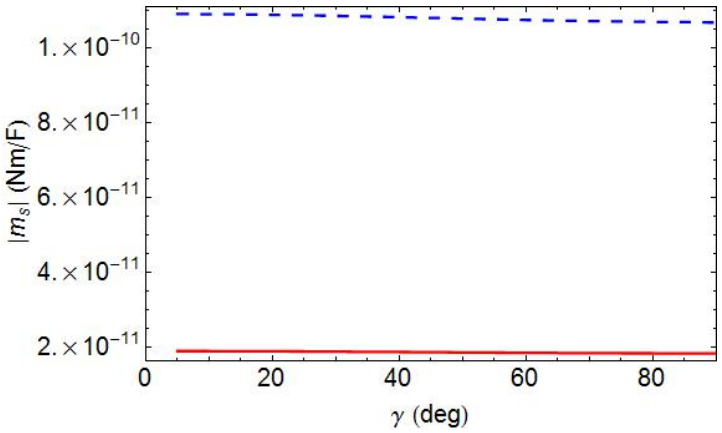

(b) Spin – Branch 1

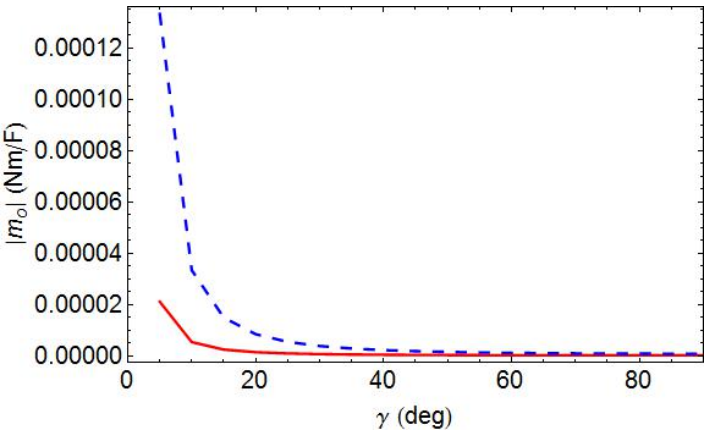

(c) Orbital – Branch 2

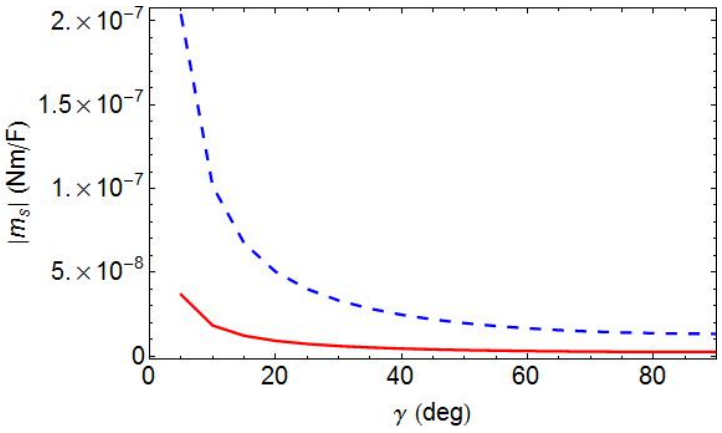

(d) Spin – Branch 2

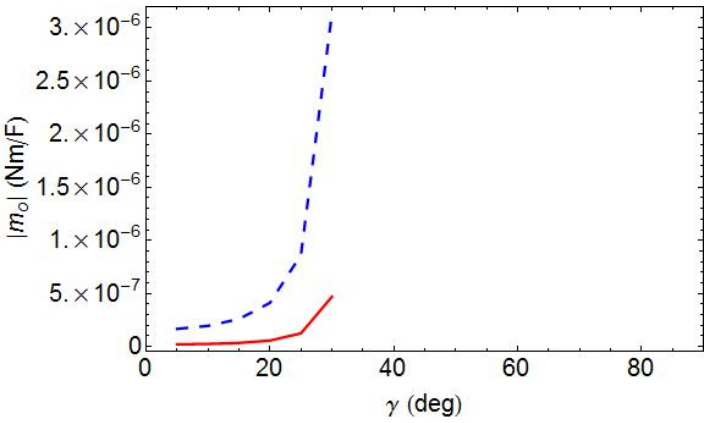

(e) Orbital – Branch 3

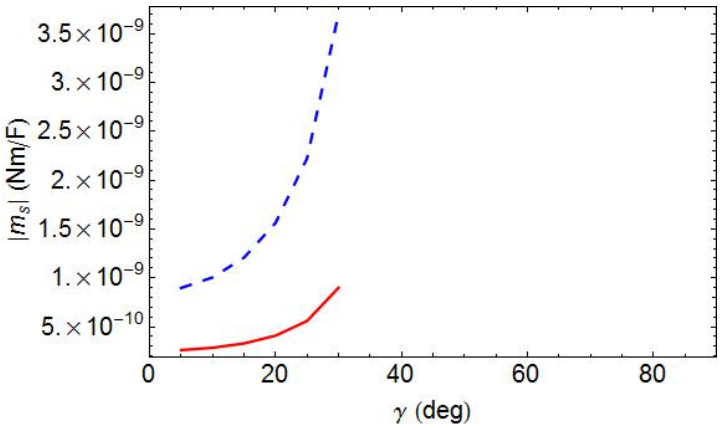

(f) Spin – Branch 3

Figure 8 The magnitudes of $\boldsymbol{m}_{s,o}^{Mink,Abr}$ as functions of γ of SPP waves guided by the interface between the bulk aluminum and the chosen titanium-oxide SNTF, when $a_p = 1V/m$. The panels (a, b), (c, d), and (e, f) correspond to the solution branches labeled 1, 2, and 3 in Figure 4. For computations, $N_d = 2$ for Branch 1, 6 for Branch 2, and 10 for Branch 3 are set after ascertaining that the values of the Cartesian components of the angular momentums are converged. Results for the Abraham and Minkowski formulations are denoted by solid red and blue-chain dashed lines, respectively.

Polarization states also play a role in influencing the magnitudes of the angular momentums. Analysis of Figure 8 and Tables 1 and 2 shows that the magnitudes of $\boldsymbol{m}_{s,o}^{Mink,Abr}$ are generally higher when the SPP waves are neither *p*- nor *s*-polarized, expect for the SPP waves on Branch 1 guided by the metal/SNTF interface. Parenthetically, we note that the polarization state of SPP waves on Branch 1 is very close to the *p*-polarization state, which may explain the lower magnitudes of the spin and orbital angular momentums of SPP waves on this branch. Of all the SPP waves guided by metal/SNTF interface, the SPP waves on Branch 2 generally have highest magnitudes of the spin and the orbital angular momentums, in both formulations.

A comparison of the results presented in Section 3.3 for the metal/CTF interface and in this section for the metal/SNTF interface shows that: (1) numerous directions are available for the angular momentums for SPP waves guided by the metal/SNTF interface in contrast to the sole SPP wave guided by the metal/CTF interface, (2) the spin and orbital angular momentums for the Branch 1 in Figure 4 for the metal/SNTF interface are comparable in magnitude with those for the sole branch in Figure 1 for the metal/CTF interface, and (3) the magnitudes of both spin and orbital angular momentums are higher by at least an order of magnitude for Branches 2 and 3 than for Branch1 in Figure 4 for the metal/SNTF interface. It should be noted that the comparison between the results for the metal/CTF and metal/SNTF interfaces is quite appropriate, because the relative permittivity dyadic of the SNTF can be transformed into the relative permittivity dyadic of the CTF by setting $\delta_v = 0^\circ$.

Chapter 4 Conclusions

The time-averaged spin and orbital parts of angular momentums of multiple SPP waves guided by the interface of a metal and a periodically nonhomogeneous SNTF were theoretically investigated using the solutions of the underlying canonical boundary-value problem. Not only do multiple SPP waves propagate with different phase speed, attenuation rate, and spatial field profiles (in particular, the degree of localization to the interface in the SNTF), but also with different magnitudes and directions of the spin and orbital parts of the angular momentum—calculated using either one of the two formulations, one due to Minkowski and the other due to Abraham. The magnitudes and directions of the angular momentums of SPP waves guided by a metal/SNTF interface can vary over large ranges.

For all SPP waves guided by the metal/SNTF interface, the orbital angular momentum lies in the interface plane and is oriented perpendicular to the direction of propagation. For some SPP waves, the spin is similarly directed. For others, the spin either lies in the plane formed by the direction of propagation and the normal to the interface or is perpendicular to the direction of propagation and the normal to the interface or is perpendicular to the direction of propagation but does not lie in the interface plane. The magnitude of the spin is less than that of the orbital angular momentum, in both formulations. Furthermore, the magnitudes of both the spin and the orbital angular momentums are higher for the SPP waves guided by the metal/SNTF interface (when the propagation of SPP waves does not take place in the morphologically significant plane) than the metal/rugate-filter interface. The magnitudes of the spin and orbital parts of the Minkowski angular momentum were found to be larger than their Abraham counterparts.

The replacement of an isotropic, homogeneous, partnering dielectric material by an isotropic, periodically nonhomogeneous, partnering dielectric material does not change the direction of the spin and orbital parts of the angular momentums of SPP waves, but the magnitudes are certainly enhanced. At the same time, periodic nonhomogeneity engenders a multiplicity of SPP waves. The replacement of an

anisotropic, homogeneous, partnering dielectric material by an anisotropic, periodically nonhomogeneous, partnering dielectric material not only engenders a multiplicity of SPP waves and significantly enhances the magnitudes of both the spin and orbital parts of the angular momentums of SPP waves, but also affords numerous directions for those quantities.

It is worth noticing in closing that the relative permittivity dyadic of the SNTF can be engineered during fabrication [29]. Therefore, the magnitudes and the directions of the spin and the orbital parts of the angular momentum can be engineered. This flexibility in the design of SNTFs—not to mention sculptured thin films of other types [29]—and the choices of the spin and the orbital angular momentums thereby available may have potential for the trapping and rotation of single molecules that infiltrate the partnering SNTF.

Appendix A: List of Notations of Physical Quantities

c	Speed of light in free space
ϵ_0	Permittivity of free space
μ_0	Permeability of free space
η_0	Characteristic impedance of free space
ω	Angular frequency of electromagnetic waves
λ_0	Wavelength of electromagnetic wave in free space
κ_0	Wavenumber of electromagnetic wave in free space
$\hbar$	Reduced Planck's constant
k_B	Boltzmann constant
$\boldsymbol{E}$	Electric field intensity
$\boldsymbol{H}$	Magnetic field intensity
$\boldsymbol{D}$	Electric displacement field
$\boldsymbol{B}$	Magnetic flux density
$\boldsymbol{M}$	Angular momentum of electromagnetic waves
$\boldsymbol{m}$	Normalized angular momentum of electromagnetic waves
$\boldsymbol{j}$	Momentum density of electromagnetic waves

Appendix B: Computer Programs for Numerical Computations

I. Newton-Raphson Method

```
function [kappa_final]= newton_raphson(omega,gamma,iter_max,kappa)
% Newton-Raphson method to solve for kappa in det[Y(kappa)]=0
lambda0=633e-9;
k0=2*pi/lambda0;
error=getY(kappa,omega,gamma);
tol=1e-16;
iter=0;
while (abs(real(error))>=tol || abs(imag(error))>=tol) && iter<iter_max
    iter=iter+1;
    kappa(iter+1)=kappa(iter)-(1e-6)*getY(kappa(iter),omega,gamma)* ...
                  kappa(iter)/(getY((1+1e-6)*kappa(iter),omega,gamma)...
                  -getY(kappa(iter),omega,gamma));
    error=getY(kappa(iter+1),omega,gamma);
end
kappa_final=kappa(iter+1);
disp('Number of iterations='); disp(iter);
end
```

II. Gauss-Legendre Quadrature

```
function [answer]=GL(momentum,kappa,omega,gamma,zmin,zmax)
% sum GLQuad over all periods in SNTF
num_period=floor(zmax/2/omega);
answer=0;
% Gauss-Legendre quadrature for all complete periods
for v=1:num_period
    answer=answer+GLQuad(momentum,kappa,omega,gamma,zmin+...
    (v-1)*2*omega,zmin+v*2*omega);
end
answer=real(answer);
end

function [quad]=GLQuad(momentum,kappa,omega,gamma,min,max)
% Gauss-Legendre Formula 32 points rule in one or less than one period
pts=32; % 32 points rule
load gl_wx  % data of weighting factors and abscissae on the axis of
interest
W=gl_wx{1,1};  % weights
A=gl_wx{1,2};  % abscissae
% Gaussian-Legendre Translation, from [min,max] to [-1,1];
Tz=((min+max)/2)+((max-min)/2)*A; % new choices of points on z axis
sum_z=0;
flag=strcmpi('sam',momentum);
if flag==1
   % disp('sntf, sam');
   for k=1:pts
```

```
        sum_z=sum_z+W(k)*sam_sntf(kappa,omega,gamma,Tz(k));
    end
    quad=(max-min)/2*sum_z;
else
    % disp('sntf, am');
    for k=1:pts
        sum_z=sum_z+W(k)*am_sntf(kappa,omega,gamma,Tz(k));
    end
    quad=(max-min)/2*sum_z;
end
end
```

REFERENCES

[1] Torres, J. P. & Torner, L. (Eds.). (2011). Twisted photons: Applications of light with orbital angular momentum. Germany: Wiley-VCH.

[2] Beth, R. (1936). Mechanical detection and measurement of the angular momentum of light. *Physics Review*, 50. doi: 10.1103/PhysRev.50.115

[3] Allen, L., Beijersbergen, M. W., Spreeuw, R. J. C., & Woerdman, J. P. (1992). Orbital angular momentum of light and the transformation of Laguerre-Gaussian laser modes. *Physics Review A*, 45, 8185-8189. doi:10.1103/PhysRevA.45.8185.

[4] Maier, S. (2007). Plasmonics: Fundamentals and applications. UK: Springer.

[5] Barnett, S. M., & Loudon, R. (2010). The enigma of optical momentum in a medium. *Phil. Trans. R. Soc. Lond. A* 368, 927–939. doi: 110.1098/rsta.2009.0207

[6] Simpson, N. B., Dholakia, K., Allen, L., Padgett, M. J. (1997). Mechanical equivalence of spin and orbital angular momentum of light: An optical spanner. *Optics Letters*, 22 (1), 52–4. doi:10.1364/OL.22.000052.

[7] Marrucci, L., Manzo, C., & Paparo, D. (2006). Optical spin-to-orbital angular momentum conversion in inhomogeneous anisotropic media. *Physical Review Letters*, 96 (16), 163905. doi:10.1103/PhysRevLett.96.163905.

[8] Kinkhabwala, A., Yu, Z., Fan, S., Avlasevich, Y., Mullen, K. & Moerner, W. E. (2009). Large single-molecule fluorescence enhancements produced by a bowtie nanoantenna. *Nature Photonics*, 3, 654-657.

[9] Homola, J. (2006). Surface plasmon resonance based sensors. Berlin: Springer.

[10] Shvets., G. & Tsukerman, I. (Eds.). (2012). Plasmonics and plasmonic metamaterials: Analysis and applications. Singapore: World Scientific.

[11] Brongersma, M. L. & Kik, P. G. (Eds.). (2007). Surface plasmon nanophotonics. The Netherlands: Springer.

[12] Lembessis, V. E., Al-Awfi, S., Babiker, M., & Andrews, D. L. (2011). Surface plasmon optical vortices and their influence on atoms. *Journal of Optics*, 13, 064002. doi:10.1088/2040-8978/13/6/064002.

[13] Liu, A., Rui, G., Ren, X., Zhan, Q., Guo, G., & Guo, G. (2012). Encoding photonic angular momentum information onto surface plasmon polaritons with plasmonic lens. *Optics Express*, 20 (22), 24151-24159. doi: 10.1364/OE.20.024151.

[14] Rury, A. & Freeling, R. (2012). Angular momentum conservation in plasmonics. Lasers and Electro-Optics (CLEO), 2012 Conference on, 1-2.

[15] Ruting, F., Fernandez-Dominguez, A. I., Martin-Moreno, L., & Garcia-Vidal, F. J. (2012). Subwavelength chiral surface plasmons that carry tuneable orbital angular momentum. *Physical Review B*, 86, 075437. doi: 10.1103/PhysRevB.86.075437.

[16] Liu, M., Zentgraf, T., Liu, Y., Bartal, G., & Zhang, X. (2010). Light-driven nanoscale plasmonic motors. *Nature Nanotechnology*, 5, 570-573. doi: 10.1038/NNANO.2010.128.

[17] Lakhtakia, A. (2011). Surface multiplasmonics. Proc. SPIE 8104, Nanostructured Thin Films IV, 810403. doi:10.1117/12.893129.

[18] Faryad, M. & Lakhtakia, A. (2010). On surface plasmon-polariton waves guided by the interface of a metal and a rugate filter with a sinusoidal refractive-index profile. *Journal of the Optical Society of America B*, 27 (11), 2218-2223.

[19] Faryad, M., Polo Jr., J. A., & Lakhtakia, A. (2010). Multiple trains of same-color surface plasmon-polaritons guided by the planar interface of a metal and a sculptured nematic thin film. Part IV: Canonical problem. *Journal of Nanophotonics*, 4, 043505, 1-11. doi: 10.1117/1.3365052.

[20] Polo Jr., J. A. & Lakhtakia, A. (2009). On the surface plasmon polariton wave at the planar interface of a metal and a chiral sculptured thin film. *Proceedings of the Royal Society of London A*,465 (2101), 87–107. doi: 10.1098/rspa.2008.0211

[21] Motyka, M. A. & Lakhtakia, A. (2008). “Multiple trains of same-color surface plasmon-polaritons guided by the planar interface of a metal and a sculptured nematic thin film,” *Journal of Nanophotonics*. 2, 021910. doi: 10.1117/1.3033757.

[22] Lakhtakia, A. (2012). Surface multiplasmonics for optical sensing and solar-energy harvesting. Microelectronics (MIEL), 2012 28th International Conference on, 41-43. doi: 10.1109/MIEL.2012.6222793

[23] Bovard, B. G. (1993). Rugate filter theory: an overview. *Applied Optics*, 32, 5427–5442. doi: 10.1364/AO.32.005427

[24] Polo, Jr., J. A. & Lakhtakia, A. (2005). Sculptured nematic thin films with periodically modulated tilt angle as rugate filters. *Optical Communications*, 251, 10-22. doi:10.1016/j.optcom.2005.02.075

[25] Motyka, M. A. & Lakhtakia, A. (2009). Multiple trains of same-color surface plasmon-polaritons guided by the planar interface of a metal and a sculptured nematic thin film. Part II: Arbitrary incidence. *Journal of Nanophotonics*, 3, 033502. doi: 10.1117/1.3147876.

[26] Lakhtakia, A., Jen, Y.-J., & Lin, C.-F. (2009). Multiple trains of same-color surface plasmon-polaritons guided by the planar interface of a metal and a sculptured nematic thin film. Part III: Experimental evidence. *Journal of Nanophotonics*, 3, 033506. doi: 10.1117/1.3249629.

[27] Faryad, M. & Lakhtakia, A. (2011). Multiple trains of same-color of surface plasmon-polaritons guided by the planar interface of a metal and a sculptured nematic thin film. Part V: Grating-coupled excitation. *Journal of Nanophotonics*. 5, 053527. doi: 10.1117/1.3365052

[28] Yakubovich, V. A. & Starzhinskii, V. M. (1975). Linear differential equations with periodic coefficients. New York: Wiley.

[29] Lakhtakia, A. & Messier, R. (2005). Sculptured thin films: Nanoengineered morphology and optics. Bellingham, WA, USA : SPIE Press.

[30] Lakhtakia, A. (2010). Reflection of an obliquely incident plane wave by a half space filled by a helicoidal bianisotropic medium. *Physics Letter A*, 374, 3887–3894.

[31] Van Enk, S. J. & Nienhuis, G. (1992). Eigenfunction description of laser beams and orbital angular momentum of light. *Optics Communications*, 94, 147–158. doi: 10.1016/0030-4018(92)90424-P

[32] Padgett, M., Barnett, S. M. & Loudon, R. (2003). The angular momentum of light inside a dielectric. *Journal of Modern Optics*, 50, 1555–1562. doi: 10.1080/09500340308235229

[33] Chapra, S. & Canale, R. (2010). Numerical methods for engineers. NY: McGraw-Hill.

[34] Kiusalaas, J. (2010). Numerical methods in engineering with MATLAB. New York: Cambridge University Press.

[35] Polo Jr., J. A. & Lakhtakia, A. (2008). Morphological effect on surface-plasmon-polariton waves at the planar interface of a metal and a columnar thin film. *Optics Communications*, 281, 5453-5457. doi: 10.1016/j.optcom.2008.07.051

[36] Mackay, T. G. & Lakhtakia, A. (2010). Electromagnetic anisotropy and bianisotropy: A field guide. Singapore: World Scientific.

[37] Hodgkinson, I. J., Wu, Q. H, & Hazel, J. (1998). Empirical equations for the principal refractive indices and column angle of obliquely deposited films of tantalum oxide, titanium oxide, and zirconium oxide. *Applied Optics*, 37, 2653–2659. doi: 10.1364/AO.37.002653.

ACADEMIC VITA

Xuerong Xiao

xxiao3e8@gmail.com

Education

The Pennsylvania State University, University Park, PA 2009-2013
B.S., Engineering Science
Minors: Nanotechnology; Electronic and Photonic Materials

Honors and Awards

- Evan Pugh Award, 2011-2013
- Sam Y. and Myrna R. Zamrik Scholarship in Engineering Science and Mechanics, 2012-2013
- Schreyer Honors College Summer Research Grant, 2012
- The Robert and Myrtle Vierck Scholarship, 2011-2012
- Schreyer Scholar, 2010-present
- Faculty Award for Academic Excellence in Engineering, 2010-2011
- President Sparks Award, 2010-2011
- Student Research Conference Presentation Honors 1st Place, 2010
- President's Freshman Award, 2009-2010

Association Memberships/Activities

- Student-Faculty Liaison, Tau Beta Pi, 2012-2013
- FTCAP Mentor, Schreyer Honors College, 2012
- Summer Close-up Panelist, Schreyer Honors College, 2012
- Student Member, The International Society for Optics and Photonics (SPIE), 2012
- Student Member, Society for Industrial and Applied Mathematics (SIAM), 2012
- Co-activities Chair, Tau Beta Pi, 2011
- Webmaster, Society of Women Engineers, 2011
- Member, Spanish Club, 2011
- Volunteer, Student Red Cross Club Blood Drive, 2011
- Photographer, "ABSENCE" (PSUGA Campus Magazine), Vol. 12, 2010
- Speaker, Teaching International Program at PSUGA, 2009
- Volunteer, THON Canning, 2009

Research Experience

- **Department of Engineering Science and Mechanics** **Spring 2012-Spring 2013**
  Studied theoretically the Minkowski and Abraham spin and orbital angular momentums of multiple surface plasmon-polaritons propagating along the planar interface between a metal and a sculpture nematic thin film, reviewed extensive literature on the theories and applications of SPPs and angular momentum of light, performed numerical modeling and analysis as senior thesis project

  Investigated effective medium theories, modeled and computed light reflection and transmission by planar multilayers of composite materials using matrix methods, statistically analyzed data

- **Applied Optoelectronics & Photonics Lab, Penn State** **Summer 2012**
  Made Christiansen filters using organic high dispersion liquids and glass particles, experimentally explored the uses of Christiansen filters for wavelength-selective transmission in optical devices

- **College of Engineering** **Spring 2011**
  Designed a tensile and bending testing lab using Wheatstone bridge circuits and strain gauges

- **Department of Mathematics** **Fall 2010**
  Developed novel techniques for finding sums of an infinite class of alternating series in a generalized form

Publications

Bohren, C. F., **Xiao, X.**, & Lakhtakia, A. (2012). The missing ingredient in effective-medium theories: standard deviations. *Journal of Modern Optics*, 59 (15), 1312-1315. doi: 10.1080/09500340.2012.713521

Chen, Z., Wei, S., & **Xiao, X**. (2011). Finding sums for an infinite class of alternating series. *International Journal of Mathematical Education in Science and Technology*, 43 (5), 694-702. doi: 10.1080/0020739X.2011.622802